An algorithm to find the optimal oriented external electrostatic field for annihilating a reaction barrier in a polarizable molecular system

The Journal of Chemical Physics

RESEARCH ARTICLE | SEPTEMBER 19 2023

An algorithm to find the optimal oriented external electrostatic field for annihilating a reaction barrier in a polarizable molecular system

Josep Maria Bofill ; Marco Severi ; Wolfgang Quapp ; Jordi Ribas-Ariño ; Ibério de P. R. Moreira ; Guillermo Albareda

J. Chem. Phys. 159, 114112 (2023)
https://doi.org/10.1063/5.0167749

The Journal of Chemical Physics ARTICLE pubs.aip.org/aip/jcp

An algorithm to find the optimal oriented external electrostatic field for annihilating a reaction barrier in a polarizable molecular system

Cite as: J. Chem. Phys. 159, 114112 (2023); doi: 10.1063/5.0167749
Submitted: 14 July 2023 • Accepted: 23 August 2023 •
Published Online: 19 September 2023

Josep Maria Bofill,[1,2,a] Marco Severi,[3] Wolfgang Quapp,[4] Jordi Ribas-Ariño,[2,5] Ibério de P. R. Moreira,[2,5] and Guillermo Albareda[6]

AFFILIATIONS

[1] Departament de Química Inorgànica i Orgànica, Secció de Química Orgànica, Universitat de Barcelona, Martí i Franquès 1, 08028 Barcelona, Spain
[2] Institut de Química Teòrica i Computacional, (IQTCUB), Universitat de Barcelona, Martí i Franquès 1, 08028 Barcelona, Spain
[3] Department of Chemistry G. Ciamician, University of Bologna, Via F. Selmi 2, 40126 Bologna, Italy
[4] Mathematisches Institut, Universität Leipzig, PF 100920, D-04009 Leipzig, Germany
[5] Departament de Ciència de Materials i Química Física, Secció de Química Física, Universitat de Barcelona, Martí i Franquès 1, 08028 Barcelona, Spain
[6] Ideaded, Carrer de la Tecnologia, 35, 08840 Viladecans, Barcelona, Spain

[a] **Author to whom correspondence should be addressed:** jmbofill@ub.edu

ABSTRACT

The use of oriented external electric fields (OEEFs) to promote and control chemical reactivity has motivated many theoretical and computational studies in the last decade to model the action of OEEFs on a molecular system and its effects on chemical processes. Given a reaction, a central goal in this research area is to predict the optimal OEEF (oOEEF) required to annihilate the reaction energy barrier with the smallest possible field strength. Here, we present a model rooted in catastrophe and optimum control theories that allows us to find the oOEEF for a given reaction valley in the potential energy surface (PES). In this model, the effective (or perturbed) PES of a polarizable molecular system is constructed by adding to the original, non-perturbed, PES a term accounting for the interaction of the OEEF with the intrinsic electric dipole and polarizability of the molecular system, so called the polarizable molecular electric dipole (PMED) model. We demonstrate that the oOEEF can be established by locating a point in the original PES with unique topological properties: the optimal barrier breakdown or bond-breaking point (oBBP). The essential feature of the oBBP structure is the fact that this point maintains its topological properties for all the applied OEEFs, also for the unperturbed PES, thus becoming much more relevant than the commonly used minima and transition state structures. The PMED model proposed here has been implemented in an open access package and is shown to successfully predict the oOEEF for two processes: an isomerization reaction of a cumulene derivative and the Huisgen cycloaddition reaction.

I. INTRODUCTION

Promotion and control of chemical reactivity of molecular systems through the utilization of oriented external electrostatic fields (OEEFs) have been a focal point of research in theoretical and computational chemistry for many years. The significant influence of external electric fields on chemical reactivity has been shown by the pioneering investigations on S_N2 reactions,[1] Friedel–Crafts reactions,[2] Diels–Alder cycloadditions,[3] C–H hydroxylations[4] and activations,[5] and C=C epoxidations.[4] A groundbreaking scanning tunneling microscopy break-junction (STM-BJ) experiment at the single-molecule level showed that the rate of a Diels–Alder reaction can be enhanced by means of an OEEF.[6] This result boosted the research on OEEF-controlled chemistry due to the great potential of using electric fields as a tool in chemical synthesis.[7–10] Indeed, recent STM-BJ experiments have demonstrated that OEEFs can accelerate the cleavage of alkoxyamine C–ON bonds,[11] two-step cascade reactions of a Diels–Alder addition followed by an aromatization process,[12] isomerization reactions of cumulenes,[13] scission of C–C bonds via electrophilic aromatic substitutions,[14] homolysis of O–O bonds in peroxyanhydrides,[15] and acylation of amines.[16] Precise details on the reaction dynamics of an OEEF-driven Diels–Alder reaction have also been obtained using single-molecule setups.[17] Besides STM-BJ experiments, other experimental techniques showing greater potential for scalability in the utilization of OEEFs for controlling reactivity[18] have been also reported.[19–24] These recent experimental works have inspired new computational investigations[10,25–46] focused on predicting and understanding how chemical reactivity and selectivity can be controlled by means of OEEFs. From a conceptual point of view, the effects of OEEFs on reactivity can be explained using valence bond approaches[7–9,26] or quantitative activation strain and Kohn–Sham molecular orbital theory.[30] In parallel to all these endeavors, recent experimental and computational works have provided strong evidence of the crucial role of local electric fields in the active sites of enzymes in defining their catalytic activity.[47–57]

In this context, the seminal work by Shaik and co-workers[3] has shown that the direction of the OEEF is a critical variable that needs to be considered when trying to maximize the effect of the field in enhancing the rate of a given reaction. According to a first-order approximation, the electric field interacts exclusively with the inherent (or intrinsic) electric dipole moment of the molecular system. Within this approximation, the direction that maximizes the catalytic effects on the molecular process[58] is given by the variation in inherent dipole moment (i.e., vector difference) between the transition state and reactants configurations of the potential energy surface (PES).[48,49] Although this approximation certainly provides a simple and quick way to predict an appropriate direction of the field, it should be stressed that it does not take into account neither polarizability effects nor electric-field-induced geometrical distortions. As such, this approximation can only be applied when the field strength is small. Indeed, larger field strengths are known to give rise to important induced dipoles and large geometrical distortions.[3,31] For this reason, it is very important to develop theoretical models that enable the prediction of the most appropriate field direction by taking into account both polarizability and geometrical perturbations. In previous works, we established the grounds of a model to find the optimal OEEF for a chemical system using catastrophe theory and optimal control.[59,60] In this model, the *optimal OEEF* (oOEEF) *is defined as the field with the smallest possible strength to render a given chemical transformation into a barrierless process*. Therefore, the oOEEF associated with a given reaction *provides the optimal electrostatic field in strength and direction to annihilate the chemical barrier*. In these works, we considered the electric field interacting with the intrinsic electric dipole moment as a perturbation of the original PES and established the main features of the oOEEF. The germ of this model is rooted in previous mechanochemistry models based on the Newton trajectory (NT) theory.[61] We showed that the oOEEF can be established once a special point of the PES is located, namely, the so-called *optimal barrier breakdown point* or, alternatively, *optimal bond breaking point* (oBBP).

In order to understand the concept of oBBP, let us consider that an OEEF is applied to drive a given reaction in the direction defined by the oOEEF to induce a continuous deformation of the original PES. For a small field strength, the reactants will be distorted in such a way that their nuclear configuration becomes closer to the transition state (TS) configuration in the perturbed PES. The TS, in turn, will be distorted in such a way that their nuclear configuration becomes closer to the reactants configuration. As the field strength increases, reactants and TS become more distorted and their configurations resemble to a larger extent. For a particular field strength (the one defined by the oOEEF), both configurations coalesce. The specific point of the perturbed PES in which the TS and reaction configurations coalesce under the action of the oOEEF is the catastrophe point called oBBP. The essential feature of the oBBP structure is the fact that this point maintains its topological properties for all the applied OEEFs, also for the unperturbed PES. Accordingly, in the context of our model, the oBBP becomes a central concept defining a new kind of special points in the unperturbed PES, much more relevant than the reactants or transition state configurations, which are commonly used to rationalize the thermochemistry of the molecular system (with or without an external electric field).

In our previous works, the nature of the oOEEF was characterized with necessary but not sufficient conditions.[59,60] This led to a cumbersome algorithm to find the oOEEF with associated numerical problems.[60] In addition to this, electric polarizability of the molecular system was not taken into account, thus preventing its use in systems where the inherent dipole is almost constant as the system evolves from reactants toward products on the PES. In an attempt to go beyond these limitations, we will establish here the necessary and sufficient conditions that an oOEEF must satisfy and use these conditions to develop a new algorithm to compute this field in an easy and efficient way, while fully taking into account the electric polarizability of the molecular system. Hence, we introduce the polarizable molecular electric dipole (PMED) model to include the effects of an OEEF on the PES of a molecular system. As will be shown below, the oOEEF can be found by first locating the oBBP on the original or unperturbed PES and then evaluating the optimal field using the first and second derivatives with respect to the atomic positions of the intrinsic electric dipole and polarizability.

This article is structured as follows: Sec. II is devoted to discuss the mathematical nature and structure of the here proposed PMED model and to prove the optimality conditions of the OEEF derived in Refs. 59 and 60. The model will first be presented for the oBBP point and will then be generalized to any non-stationary point of the

original or unperturbed PES (in Appendices A and B). The numerical analysis of a generic two-dimensional model system allows one to deeply understand the full nature of the model and its generalization. In Sec. III, we report the application of the algorithm to two real chemical examples, described in Subsections III A and III B. Finally, the main conclusions of the present study are reported in Sec. IV.

II. MATHEMATICAL BACKGROUND OF THE POLARIZABLE MOLECULAR ELECTRIC DIPOLE (PMED) MODEL

A. Mathematical formulation of the PMED model

A general model to describe the action of an OEEF given by $\mathbf{e} = (\varepsilon_x, \varepsilon_y, \varepsilon_z) = E\mathbf{e}_n$ (with modulus E and normalized direction $\mathbf{e}_n$) on a molecular system is provided by the polarizable molecular electric dipole (PMED) ansatz[59] as

$$\begin{aligned} V_{\mathbf{e}_n}(\mathbf{x}, E) &= V(\mathbf{x}) + P_{\mathbf{e}_n}(\mathbf{x}, E) \\ &= V(\mathbf{x}) - E\mathbf{e}_n^T\{\mathbf{d}(\mathbf{x}) + 1/2\mathbf{A}(\mathbf{x})\mathbf{e}_n E\}. \end{aligned} \tag{1}$$

In this expression, $V(\mathbf{x})$ is the original PES, $P_{\mathbf{e}_n}(\mathbf{x}, E)$ is the (electrostatic) perturbation energy, $\mathbf{d}(\mathbf{x})$ is the electric dipole moment vector, $\mathbf{x}^T = (x_1, y_1, z_1, \ldots, x_M, y_M, z_M)$ is the vector of the Cartesian coordinates of all M atoms of the system, and $\mathbf{e}_n^T = (e_x, e_y, e_z)$ is the three-dimensional normalized field direction vector of the applied OEEF. We recall that the electric dipole moment is a three-component vector, where each component is dependent (in a nonlinear manner) on the $\mathbf{x}$-vector, $\mathbf{d}^T(\mathbf{x}) = (d_x(\mathbf{x}), d_y(\mathbf{x}), d_z(\mathbf{x}))$, whereas $\mathbf{A}(\mathbf{x})$ is the electric polarizability tensor given by a 3×3 symmetric matrix, where each component, $a_{i,j}(\mathbf{x})$ for $i, j = x, y, z$, is also nonlinearly dependent on the $\mathbf{x}$-vector. Note that the present model assumes that the molecular system is under an homogeneous electric field, that is, $\mathbf{e}$ is independent of $\mathbf{x}$. This would correspond to an experimental setup in which the molecular system is oriented inside a large capacitor. Therefore, the model neglects the inhomogeneities of the electric field that emerge in other experimental setups, such as STM junctions[62] and active sites of enzymes.[63]

We also assume that $V(\mathbf{x})$, $d_i(\mathbf{x})$, and $a_{i,j}(\mathbf{x})$ are "well-behaved" functions of $\mathbf{x}$; thus, they have continuous second derivatives with $[\nabla_{\mathbf{x}}\nabla_{\mathbf{x}}^T V(\mathbf{x})] = [\nabla_{\mathbf{x}}\nabla_{\mathbf{x}}^T V(\mathbf{x})]^T$, $[\nabla_{\mathbf{x}}\nabla_{\mathbf{x}}^T d_i(\mathbf{x})] = [\nabla_{\mathbf{x}}\nabla_{\mathbf{x}}^T d_i(\mathbf{x})]^T$, and $[\nabla_{\mathbf{x}}\nabla_{\mathbf{x}}^T a_{i,j}(\mathbf{x})] = [\nabla_{\mathbf{x}}\nabla_{\mathbf{x}}^T a_{i,j}(\mathbf{x})]^T$ for $i, j = x, y, z$, where $\nabla_{\mathbf{x}}^T = (\partial/\partial x_1, \ldots, \partial/\partial z_M)$. The stationary condition on $V_{\mathbf{e}_n}(\mathbf{x}, E)$ reads

$$\begin{aligned} \nabla_{\mathbf{x}} V_{\mathbf{e}_n}(\mathbf{x}, E) &= \nabla_{\mathbf{x}} V(\mathbf{x}) + \nabla_{\mathbf{x}} P_{\mathbf{e}_n}(\mathbf{x}, E) \\ &= \nabla_{\mathbf{x}} V(\mathbf{x}) - \Big\{[\nabla_{\mathbf{x}}\mathbf{d}^T(\mathbf{x})] \\ &\quad + 1/2E[\nabla_{\mathbf{x}}[\mathbf{A}(\mathbf{x})\mathbf{e}_n]^T]\Big\}\mathbf{e}_n E \\ &= \mathbf{0}. \end{aligned} \tag{2}$$

It is useful to define the vectors

$$\mathbf{h}_{\mathbf{e}_n}(\mathbf{x}) = [\nabla_{\mathbf{x}}\mathbf{d}^T(\mathbf{x})]\mathbf{e}_n = \sum_{i=(x,y,z)} e_i(\nabla_{\mathbf{x}} d_i(\mathbf{x})) \tag{3}$$

and

$$\mathbf{f}_{\mathbf{e}_n}(\mathbf{x}) = \mathbf{A}(\mathbf{x})\mathbf{e}_n = \sum_{i=(x,y,z)} e_i\mathbf{a}_i(\mathbf{x}), \tag{4}$$

where $\mathbf{a}_i(\mathbf{x})$ is the i-column of the $\mathbf{A}(\mathbf{x})$ matrix, namely, $\mathbf{a}_i^T(\mathbf{x}) = (a_{x,i}(\mathbf{x}), a_{y,i}(\mathbf{x}), a_{z,i}(\mathbf{x}))$, and

$$\begin{aligned} \mathbf{p}_{\mathbf{e}_n}(\mathbf{x}) &= [\nabla_{\mathbf{x}}\mathbf{f}_{\mathbf{e}_n}^T(\mathbf{x})]\mathbf{e}_n \\ &= \sum_{i=(x,y,z)} e_i(\nabla_{\mathbf{x}} f_{\mathbf{e}_n i}(\mathbf{x})) \\ &= \sum_{i=(x,y,z)} e_i\left(\sum_{j=(x,y,z)} e_j(\nabla_{\mathbf{x}} a_{i,j}(\mathbf{x}))\right), \end{aligned} \tag{5}$$

with $f_{\mathbf{e}_n i}(\mathbf{x})$ being the i component of the three-dimensional $\mathbf{f}_{\mathbf{e}_n}(\mathbf{x})$ vector, and finally, $\mathbf{g}(\mathbf{x}) = \nabla_{\mathbf{x}} V(\mathbf{x})$. With these definitions, we rewrite Eq. (2) in a more compact form as

$$\mathbf{g}(\mathbf{x}) - [\mathbf{h}_{\mathbf{e}_n}(\mathbf{x})E + 1/2\mathbf{p}_{\mathbf{e}_n}(\mathbf{x})E^2] = \mathbf{g}(\mathbf{x}) + \mathbf{m}_{\mathbf{e}_n}(\mathbf{x}, E) = \mathbf{0}. \tag{6}$$

We note that

$$-[\mathbf{h}_{\mathbf{e}_n}(\mathbf{x})E + 1/2\mathbf{p}_{\mathbf{e}_n}(\mathbf{x})E^2] = \mathbf{m}_{\mathbf{e}_n}(\mathbf{x}, E) = \nabla_{\mathbf{x}} P_{\mathbf{e}_n}(\mathbf{x}, E) \tag{7}$$

is the gradient of $P_{\mathbf{e}_n}(\mathbf{x}, E)$ with respect to $\mathbf{x}$, which is a quadratic vectorial function in the E parameter. Let us consider a given normalized constant vector $\mathbf{e}_n$; then, the set of points $(\mathbf{x}, E)$ satisfying Eq. (6) is called the force displaced stationary point (FDSP) curve. At each point of this curve, $(\mathbf{x}(t), E(t))$, where t is the parameter that characterizes the curve, an effective PES, $V_{\mathbf{e}_n}(\mathbf{x}, E(t))$, is generated that satisfies the stationary condition in Eq. (6). Thus, for each normalized $\mathbf{e}_n$-vector, the corresponding FDSP curve generates a sequence of $V_{\mathbf{e}_n}(\mathbf{x}, E)$ effective potentials, and each effective potential has its own fixed E, the $\mathbf{x}$ coordinates being the set of variables. In other words, for each effective potential in the sequence, the set of coordinates $\mathbf{x}$ plays the role of variables, whereas the intensity E plays the role of a parameter. The FDSP curve is a generalized NT curve where the intensity of field E changes at each point to satisfy Eq. (6). It is interesting to note that the normalized vector $\mathbf{e}_n$ plays the role of the control axis and the intensity (or strength) E is the control parameter. Here, we emphasize that the effective energy potential, $V_{\mathbf{e}_n}(\mathbf{x}, E)$, can be seen as a function of the set of variables $\mathbf{x}$ and the parameter E. When the control variable E has a fixed value, the system settles into a structure where the variables $\mathbf{x}$ stationarize (locally) the function $V_{\mathbf{e}_n}(\mathbf{x}, E)$. In particular, the current point $\mathbf{x}(t)$ of the FDSP curve corresponding to the control axis $\mathbf{e}_n$ is a stationary point of $V_{\mathbf{e}_n}(\mathbf{x}, E)$ since this point satisfies Eq. (6) for the current control parameter $E(t)$. As the control variable changes, namely, from $E(t)$ to $E(t + \Delta t)$, a local stationary point can disappear and the variables $\mathbf{x}$ jump suddenly to a different structure. In particular, the current stationary point changes from $\mathbf{x}(t)$ to a new point, $\mathbf{x}(t + \Delta t)$, satisfying Eq. (6) for the new $E(t + \Delta t)$. In a similar manner, for a given normalized $\mathbf{e}_n$-vector, the manifold of points satisfying $\det[\mathbf{H}_{\mathbf{e}_n}(\mathbf{x}, E)] = 0$ varies as the control parameter E varies, where $\mathbf{H}_{\mathbf{e}_n}(\mathbf{x}, E) = \nabla_{\mathbf{x}}\nabla_{\mathbf{x}}^T V_{\mathbf{e}_n}(\mathbf{x}, E)$ is the Hessian matrix of $V_{\mathbf{e}_n}(\mathbf{x}, E)$. We search for the E parameter associated with a given normalized $\mathbf{e}_n$-vector where the corresponding FDSP point $\mathbf{x}$ is also a point belonging to the manifold $\det[\mathbf{H}_{\mathbf{e}_n}(\mathbf{x}, E)] = 0$; this point $\mathbf{x}$ is

a degenerate stationary point of the current $V_{\mathbf{e}_n}(\mathbf{x},E)$. The structure of $V_{\mathbf{e}_n}(\mathbf{x},E)$ around this point is the object of analysis of catastrophe theory and has a shoulder form. In the present context, we call this point Bond-Breaking-Point (BBP) $(\mathbf{x}_{BBP},E_{BBP})$ associated with the control axis $\mathbf{e}_n$. The explanation given above is represented schematically in Fig. 1 of Ref. 60.

In order to obtain an analytical expression to calculate the FDSP curve associated with a given $\mathbf{e}_n$-vector, we use the implicit function theorem[64] applied to the expression $d(\nabla_{\mathbf{x}}V_{\mathbf{e}_n}(\mathbf{x},E))/dt=\mathbf{0}$. This leads to the differential equation,[59,60]

$$\mathbf{H}_{\mathbf{e}_n}(\mathbf{x},E)\left(\frac{d\mathbf{x}}{dt}\right)=\mathbf{r}_{\mathbf{e}_n}(\mathbf{x},E)\left(\frac{dE}{dt}\right). \tag{8}$$

In this expression, the $\mathbf{r}_{\mathbf{e}_n}(\mathbf{x},E)$ vector is

$$\mathbf{r}_{\mathbf{e}_n}(\mathbf{x},E)=\mathbf{h}_{\mathbf{e}_n}(\mathbf{x})+E\mathbf{p}_{\mathbf{e}_n}(\mathbf{x}), \tag{9}$$

as will be shown below. The explicit form of the Hessian matrix reads

$$\mathbf{H}_{\mathbf{e}_n}(\mathbf{x},E)=\mathbf{H}(\mathbf{x})-\mathbf{F}_{\mathbf{e}_n}(\mathbf{x},E), \tag{10}$$

being $\mathbf{H}(\mathbf{x})=\nabla_{\mathbf{x}}\nabla_{\mathbf{x}}^{T}V(\mathbf{x})$ the Hessian matrix of the original PES, $V(\mathbf{x})$, and

$$\begin{aligned}\mathbf{F}_{\mathbf{e}_n}(\mathbf{x},E)&=E\nabla_{\mathbf{x}}\mathbf{h}_{\mathbf{e}_n}^{T}(\mathbf{x})+\frac{1}{2}E^2\nabla_{\mathbf{x}}\mathbf{p}_{\mathbf{e}_n}^{T}(\mathbf{x})\\&=E\sum_{i=(x,y,z)}e_i\left[(\nabla_{\mathbf{x}}\nabla_{\mathbf{x}}^{T}d_i(\mathbf{x}))+\frac{E}{2}(\nabla_{\mathbf{x}}\nabla_{\mathbf{x}}^{T}f_{\mathbf{e}_n i}(\mathbf{x}))\right]\\&=\sum_{i=(x,y,z)}\varepsilon_i\mathbf{M}_i(\mathbf{x},\mathbf{e}).\end{aligned} \tag{11}$$

We note that $-\mathbf{F}_{\mathbf{e}_n}(\mathbf{x},E)=\nabla_{\mathbf{x}}\nabla_{\mathbf{x}}^{T}P_{\mathbf{e}_n}(\mathbf{x},E)$. Equations (3) and (5) are used in the development of Eq. (11). The specific form of $\nabla_{\mathbf{x}}\nabla_{\mathbf{x}}^{T}f_{\mathbf{e}_n i}(\mathbf{x})$ appearing in Eq. (11) is

$$\nabla_{\mathbf{x}}\nabla_{\mathbf{x}}^{T}f_{\mathbf{e}_n i}(\mathbf{x})=\sum_{j=(x,y,z)}e_j(\nabla_{\mathbf{x}}\nabla_{\mathbf{x}}^{T}a_{i,j}(\mathbf{x})),\quad i=x,y,z. \tag{12}$$

Finally, the expression of $\mathbf{r}_{\mathbf{e}_n}(\mathbf{x},E)$ vector given in Eq. (8) is obtained. We recall that the vector

$$\begin{aligned}-\mathbf{r}_{\mathbf{e}_n}(\mathbf{x},E)&=\partial(\nabla_{\mathbf{x}}V_{\mathbf{e}_n}(\mathbf{x},E))/\partial E\\&=\partial(\nabla_{\mathbf{x}}P_{\mathbf{e}_n}(\mathbf{x},E))/\partial E\\&=\partial(\mathbf{m}_{\mathbf{e}_n}(\mathbf{x},E))/\partial E\end{aligned} \tag{13}$$

and that

$$\partial V_{\mathbf{e}_n}(\mathbf{x},E)/\partial E=\partial P_{\mathbf{e}_n}(\mathbf{x},E)/\partial E=-\mathbf{e}_n^{T}[\mathbf{d}(\mathbf{x})+E\mathbf{A}(\mathbf{x})\mathbf{e}_n]$$

and

$$\partial^2 V_{\mathbf{e}_n}(\mathbf{x},E)/\partial E^2=\partial^2 P_{\mathbf{e}_n}(\mathbf{x},E)/\partial E^2=-\mathbf{e}_n^{T}\mathbf{A}(\mathbf{x})\mathbf{e}_n,$$

which recover the first- and second-order terms in the multipolar development of the molecular charge distribution assumed by the PMED ansatz in Eq. (1). Note that these two terms are not necessary for the development of the present theory. We note that the Hessian matrix, $\mathbf{H}_{\mathbf{e}_n}(\mathbf{x},E)$, is symmetric since $\mathbf{H}(\mathbf{x})$ and $-\mathbf{F}_{\mathbf{e}_n}(\mathbf{x},E)$ are symmetric matrices. Equation (8) tells us how the planes tangent to the iso-contours, $V(\mathbf{x})=v$ and $P_{\mathbf{e}_n}(\mathbf{x},E)=\pi$, with parallel normals, $\mathbf{g}(\mathbf{x})$ and $\mathbf{m}_{\mathbf{e}_n}(\mathbf{x},E)$, respectively, are transported through the FDSP curve associated with the field $\mathbf{e}_n$.

Along the integration of Eq. (8), one finds a point where $\det[\mathbf{H}_{\mathbf{e}_n}(\mathbf{x},E)]=0$, implying that an eigenvector of $\mathbf{H}_{\mathbf{e}_n}(\mathbf{x},E)$ has a null eigenvalue. When this occurs at a point of the FDSP curve, the eigenvector with a null eigenvalue of $\mathbf{H}_{\mathbf{e}_n}(\mathbf{x},E)$ is taken as normalized tangent vector, $d\mathbf{x}/dt$.[59,60] Regarding Eq. (8), with this tangent, the left hand-side part becomes zero and simultaneously dE/dt tends to zero. Thus, at the point $(\mathbf{x}^T,E)$ of the FDSP curve where $\det[\mathbf{H}_{\mathbf{e}_n}(\mathbf{x},E)]=0$, the electric field intensity (or strength) E shows a turning point. This point is labeled *barrier breakdown or bond-breaking point* (BBP), $\mathbf{x}_{BBP}$, and the intensity of the field is labeled E_{BBP}. As explained above, this point is a degenerate stationary point since it belongs to the manifold of points where $\det[\mathbf{H}_{\mathbf{e}_n}(\mathbf{x},E_{BBP})]=0$ of the current $V_{\mathbf{e}_n}(\mathbf{x},E_{BBP})$ (see Fig. 1 of Ref. 60).

B. Defining the optimal oriented external electric field

Within the manifold of BBPs of the modified PES, $V_{\mathbf{e}_n}(\mathbf{x},E)$, there is an optimal BBP. This BBP defines the optimal force in magnitude and direction that should be applied to a molecular system to promote a given chemical transformation by means of an electric field. The electric force to be applied to the molecular system is $\mathbf{m}_{\mathbf{e}_n}(\mathbf{x},E)$ [see Eq. (7)] and $-\mathbf{m}_{\mathbf{e}_n}(\mathbf{x},E)=\mathbf{g}(\mathbf{x})$. All the different FDSP curves that leave from the minimum in the perturbed PES corresponding to the reactants and arrive to the same stationary point cross at least once a $\det[\mathbf{H}(\mathbf{x})]=0$-manifold. The FDSP curve that crosses this manifold at the point where the square of the gradient norm, $\mathbf{g}^T(\mathbf{x})\mathbf{g}(\mathbf{x})$, is minimum within the iso-contour, $V(\mathbf{x})=v$, is *optimal* with respect to $\mathbf{x}$, and this point is the *optimal BBP* (oBBP). Thus, the *optimal BBP* should satisfy the condition

$$\mathbf{H}(\mathbf{x})\mathbf{g}(\mathbf{x})=\mathbf{0},\quad \mathbf{g}(\mathbf{x})\neq\mathbf{0}. \tag{14}$$

The optimal BBP point coincides with a point of the gradient extremal (GE)[65–75] of the original PES, $V(\mathbf{x})$. We recall that Eq. (14) is an eigenvalue equation where the eigenvalue of the eigenvector $\mathbf{g}(\mathbf{x})$ is zero; this is the reason why in this point $\det[\mathbf{H}(\mathbf{x})]=0$. The location of optimal BBPs in the unperturbed PES is extremely important in the context of the present model because these points reveal which is the most efficient way to trigger a reaction by means of an external electric field. The methods to find oBBPs have been already published in Refs. 76 and 77 and can be routinely used as an interface with standard molecular electronic structure packages.

Once the oBBP has been located, the work that remains to be done is to find the oOEEF (the optimal OEEF). For this purpose, we need an analysis of the BBP condition. According to Subsection II A, at the BBP, $(\mathbf{x}_{BBP}^T,E_{BBP})$, the next two conditions are satisfied,

$$\left.\frac{dE}{dt}\right|_{E=E_{BBP}}=0, \tag{15a}$$

$$\mathbf{H}_{\mathbf{e}_n}(\mathbf{x},E)\left(\frac{d\mathbf{x}}{dt}\right)\Bigg|_{\substack{\mathbf{x}=\mathbf{x}_{BBP}\\E=E_{BBP}}}=\mathbf{0}. \tag{15b}$$

If we substitute Eq. (10) into Eq. (15b), using the resolution of identity and dividing by the tangent norm, we have

$$\left(\mathbf{I}-\frac{\dot{\mathbf{x}}\dot{\mathbf{x}}^T}{\dot{\mathbf{x}}^T\dot{\mathbf{x}}}\right)[\mathbf{H}(\mathbf{x}_{BBP})-\mathbf{F}_{\mathbf{e}_n}(\mathbf{x}_{BBP},E_{BBP})]\frac{\dot{\mathbf{x}}}{\sqrt{\dot{\mathbf{x}}^T\dot{\mathbf{x}}}} + \left(\frac{\dot{\mathbf{x}}\dot{\mathbf{x}}^T}{\dot{\mathbf{x}}^T\dot{\mathbf{x}}}\right)[\mathbf{H}(\mathbf{x}_{BBP})-\mathbf{F}_{\mathbf{e}_n}(\mathbf{x}_{BBP},E_{BBP})]\frac{\dot{\mathbf{x}}}{\sqrt{\dot{\mathbf{x}}^T\dot{\mathbf{x}}}}=\mathbf{0}, \quad (16)$$

where $\dot{\mathbf{x}}=d\mathbf{x}/dt$. Equation (16) states that at the BBP, the tangent $\dot{\mathbf{x}}$ is an eigenvector of the effective Hessian, $\mathbf{H}_{\mathbf{e}_n}(\mathbf{x},E)$, defined in Eq. (10). Thus, the two expectation values, namely, $\dot{\mathbf{x}}^T\mathbf{H}(\mathbf{x}_{BBP})\dot{\mathbf{x}}/(\dot{\mathbf{x}}^T\dot{\mathbf{x}})$ and $-\dot{\mathbf{x}}^T\mathbf{F}_{\mathbf{e}_n}(\mathbf{x}_{BBP},E_{BBP})\dot{\mathbf{x}}/(\dot{\mathbf{x}}^T\dot{\mathbf{x}})$, must be equal but opposite in sign at the BBP, $(\mathbf{x}_{BBP}^T,E_{BBP})$, implying that $\dot{\mathbf{x}}^T\mathbf{H}_{\mathbf{e}_n}(\mathbf{x}_{BBP},E_{BBP})\dot{\mathbf{x}}/(\dot{\mathbf{x}}^T\dot{\mathbf{x}})=0$. We conclude that $V(\mathbf{x})$ and $P_{\mathbf{e}_n}(\mathbf{x},E)$ are functions whose first and second derivatives with respect to $\mathbf{x}$ coincide but with opposite sign at the BBP. Taking into account that *two functions are said to have contact order two* if the first and second derivatives of these functions coincide in this point,[60] we can conclude that the $\mathbf{x}=\mathbf{x}_{BBP}$ point is the contact point of order two of the $V(\mathbf{x})$ and $P_{\mathbf{e}_n}(\mathbf{x},E)$ functions for $E=E_{BBP}$. This is the essential property of BBPs for the present development based on catastrophe and control theories.

Now, we consider the case that the tangent vector $\dot{\mathbf{x}}$ coincides with the parallel normals $\mathbf{g}(\mathbf{x})$ and $\mathbf{m}_{\mathbf{e}_n}(\mathbf{x},E)$ in the BBP. In this case, the relation

$$\frac{\dot{\mathbf{x}}}{\sqrt{\dot{\mathbf{x}}^T\dot{\mathbf{x}}}}=\frac{\mathbf{g}(\mathbf{x}_{BBP})}{\sqrt{\mathbf{g}^T(\mathbf{x}_{BBP})\mathbf{g}(\mathbf{x}_{BBP})}} =-\frac{\mathbf{m}_{\mathbf{e}_n}(\mathbf{x}_{BBP},E_{BBP})}{\sqrt{\mathbf{m}_{\mathbf{e}_n}^T(\mathbf{x}_{BBP},E_{BBP})\mathbf{m}_{\mathbf{e}_n}(\mathbf{x}_{BBP},E_{BBP})}} \quad (17)$$

holds since BBP is a point of a FDSP curve and Eq. (6) should be satisfied. Equation (17) allows us to rewrite Eq. (15) in the following form:[59]

$$\left.\frac{dE}{dt}\right|_{E=E_{BBP}}=0, \quad (18a)$$

$$\mathbf{H}_{\mathbf{e}_n}(\mathbf{x},E)\left(\frac{\mathbf{g}(\mathbf{x})}{\sqrt{\mathbf{g}^T(\mathbf{x})\mathbf{g}(\mathbf{x})}}\right)\Bigg|_{\begin{pmatrix}\mathbf{x}=\mathbf{x}_{BBP}\\ E=E_{BBP}\end{pmatrix}}=\mathbf{0}, \qquad \mathbf{g}(\mathbf{x})\neq\mathbf{0}. \quad (18b)$$

We note that in Eq. (18b), $1/\sqrt{\mathbf{g}^T(\mathbf{x})\mathbf{g}(\mathbf{x})}$ enters as a normalization factor since it is an eigenvalue equation where the gradient vector, $\mathbf{g}(\mathbf{x})$, which is different to the zero vector, is the eigenvector of the null eigenvalue of the matrix, $\mathbf{H}_{\mathbf{e}_n}(\mathbf{x},E)$, at the point, $(\mathbf{x},E)=(\mathbf{x}_{BBP},E_{BBP})$. Taking into account this fact and the first term of the left-hand side part of Eq. (16), we can rewrite this equation in a decoupled form as

$$\mathbf{k}(\mathbf{x})=\left[\mathbf{I}-\frac{\mathbf{g}(\mathbf{x})\mathbf{g}^T(\mathbf{x})}{\mathbf{g}^T(\mathbf{x})\mathbf{g}(\mathbf{x})}\right]\mathbf{H}(\mathbf{x})\frac{\mathbf{g}(\mathbf{x})}{\sqrt{\mathbf{g}^T(\mathbf{x})\mathbf{g}(\mathbf{x})}} =\left[\mathbf{I}-\frac{\mathbf{g}(\mathbf{x})\mathbf{g}^T(\mathbf{x})}{\mathbf{g}^T(\mathbf{x})\mathbf{g}(\mathbf{x})}\right]\mathbf{F}_{\mathbf{e}_n}(\mathbf{x},E)\frac{\mathbf{g}(\mathbf{x})}{\sqrt{\mathbf{g}^T(\mathbf{x})\mathbf{g}(\mathbf{x})}}, \quad (19a)$$

$$\frac{\mathbf{g}(\mathbf{x})}{\sqrt{\mathbf{g}^T(\mathbf{x})\mathbf{g}(\mathbf{x})}}k(\mathbf{x})=\frac{\mathbf{g}(\mathbf{x})}{\sqrt{\mathbf{g}^T(\mathbf{x})\mathbf{g}(\mathbf{x})}}\frac{\mathbf{g}^T(\mathbf{x})\mathbf{H}(\mathbf{x})\mathbf{g}(\mathbf{x})}{\mathbf{g}^T(\mathbf{x})\mathbf{g}(\mathbf{x})} =\frac{\mathbf{g}(\mathbf{x})}{\sqrt{\mathbf{g}^T(\mathbf{x})\mathbf{g}(\mathbf{x})}}\frac{\mathbf{g}^T(\mathbf{x})\mathbf{F}_{\mathbf{e}_n}(\mathbf{x},E)\mathbf{g}(\mathbf{x})}{\mathbf{g}^T(\mathbf{x})\mathbf{g}(\mathbf{x})}, \quad (19b)$$

where we use $k(\mathbf{x})=\mathbf{g}^T(\mathbf{x})\mathbf{H}(\mathbf{x})\mathbf{g}(\mathbf{x})/(\mathbf{g}^T(\mathbf{x})\mathbf{g}(\mathbf{x}))=\mathbf{g}^T(\mathbf{x})\mathbf{F}_{\mathbf{e}_n}(\mathbf{x},E)\mathbf{g}(\mathbf{x})/(\mathbf{g}^T(\mathbf{x})\mathbf{g}(\mathbf{x}))$.

Equations (19) tell us that this class of BBP can be related with points of gradient extremal (GE)[65–75] curves if both sides of the equality that appears in Eq. (19a) are equal to zero, $\mathbf{k}(\mathbf{x})=\mathbf{0}$. The GEs are curves that usually run along valley floors or ridges of a PES. More rigorously, the GE curves of the original PES, $V(\mathbf{x})$, are defined as the curves, $\mathbf{x}(t)$, where t is the curve parameter, which cut at each point a member of the isopotential hypersurfaces of this PES, $V(\mathbf{x}(t))=v(t)$. The square of the gradient norm, $\nabla_{\mathbf{x}}^T V(\mathbf{x})\nabla_{\mathbf{x}}V(\mathbf{x})=\mathbf{g}^T(\mathbf{x})\mathbf{g}(\mathbf{x})$, is stationary at each point of this curve with respect to the variations of $\mathbf{x}$ within the member of isopotential hypersurfaces that is cut by the curve at this point. The same concept can be applied to the perturbation potential, $P_{\mathbf{e}_n}(\mathbf{x},E)$, where in this case the GE curve cuts the isopotential hypersurfaces, $P_{\mathbf{e}_n}(\mathbf{x}(t),E)=\pi(t)$. The corresponding square of the gradient norm, $\nabla_{\mathbf{x}}^T P_{\mathbf{e}_n}(\mathbf{x},E)\nabla_{\mathbf{x}}P_{\mathbf{e}_n}(\mathbf{x},E)=\mathbf{m}_{\mathbf{e}_n}^T(\mathbf{x},E)\mathbf{m}_{\mathbf{e}_n}(\mathbf{x},E)$, is stationary at each point of this curve with respect to the variations of $\mathbf{x}$ within the member of isopotential hypersurfaces that is cut by the curve at this point. The condition satisfying GE requirements for both $V(\mathbf{x})$ and $P_{\mathbf{e}_n}(\mathbf{x},E)$ functions are

$$\left[\mathbf{I}-\frac{\mathbf{g}(\mathbf{x})\mathbf{g}^T(\mathbf{x})}{\mathbf{g}^T(\mathbf{x})\mathbf{g}(\mathbf{x})}\right]\mathbf{H}(\mathbf{x})\frac{\mathbf{g}(\mathbf{x})}{\sqrt{\mathbf{g}^T(\mathbf{x})\mathbf{g}(\mathbf{x})}}=\mathbf{0}, \quad (20a)$$

$$\left[\mathbf{I}-\frac{\mathbf{m}_{\mathbf{e}_n}(\mathbf{x},E)\mathbf{m}_{\mathbf{e}_n}^T(\mathbf{x},E)}{\mathbf{m}_{\mathbf{e}_n}^T(\mathbf{x},E)\mathbf{m}_{\mathbf{e}_n}(\mathbf{x},E)}\right]\mathbf{F}_{\mathbf{e}_n}(\mathbf{x},E) \times\frac{\mathbf{m}_{\mathbf{e}_n}(\mathbf{x},E)}{\sqrt{\mathbf{m}_{\mathbf{e}_n}^T(\mathbf{x},E)\mathbf{m}_{\mathbf{e}_n}(\mathbf{x},E)}}=\mathbf{0}, \quad (20b)$$

respectively. If we assume that Eqs. (20) can be satisfied at the class of point $(\mathbf{x},E)=(\mathbf{x}_{BBP},E_{BBP})$ of the effective PES, where the tangent, $\dot{\mathbf{x}}$, of the FDSP curve at this point is collinear with the gradients of $V(\mathbf{x})$ and $P_{\mathbf{e}_n}(\mathbf{x},E)$ functions, then Eq. (17) is satisfied and the two expressions (20) coincide with the two right-hand side terms of Eq. (19a), both sides of this equation being equal to zero, and thus, $\mathbf{k}(\mathbf{x})=\mathbf{0}$. Hence, in the set of BBPs, $(\mathbf{x}_{BBP},E_{BBP})$, where (i) the tangent vector of the FDSP curve, $\dot{\mathbf{x}}$, is collinear to the gradient $\mathbf{g}(\mathbf{x})$ and (ii) the point $\mathbf{x}_{BBP}$ belongs to a point of GE curve of $V(\mathbf{x})$ function, the left-hand side part of Eq. (19a) is zero, and due to this equality, this point is also a GE point of the $P_{\mathbf{e}_n}(\mathbf{x},E)$ function and vice versa. The eigenvalues are equal but opposite in sign, according Eq. (19b). In other words, in this class of BBP, the two functions $V(\mathbf{x})$ and $P_{\mathbf{e}_n}(\mathbf{x},E)$ are contact of order two and the point is a GE of both functions.

Each point of a GE curve possesses optimal properties already described in Refs. 69 and 75. The most important property is that the

gradient norm is stationary with respect to variations in $\mathbf{x}$ within the isopotential hypersurface. In its ascent evolution from a minimum, there is a point of the GE curve where the eigenvalue of the gradient eigenvector is zero; thus, $k(\mathbf{x}) = 0$. In this point, the GE curve is crossing the $\det[\mathbf{H}(\mathbf{x})] = 0$ manifold. This point of the GE curve is where the square of the gradient norm, $\mathbf{g}^T(\mathbf{x})\mathbf{g}(\mathbf{x})$, takes a stationary value with respect to the GE tangent vector projected on the gradient vector. For this reason, this square of the gradient norm is stationary not only in all the independent directions contained in the isopotential hypersurface but also in directions that transverse this isopotential manifold. Thus, the square of the gradient norm is stationary in this point with respect to all independent directions.[78] If this point is taken as a BBP of a FDSP curve, the gradient vector and its norm of this point indicate the lowest electrical force, $\mathbf{m}_{\mathbf{e}_n}(\mathbf{x}, E)$, in magnitude and the corresponding optimal direction that should be applied to a molecular system in order to promote a given chemical transformation by an applied electric field. For this reason, the FDSP path that passes through a BBP where the tangent vector, $\dot{\mathbf{x}}$, is parallel to the gradients of $V(\mathbf{x})$ and $P_{\mathbf{e}_n}(\mathbf{x}, E)$ and satisfies the GE condition [i.e., $\mathbf{k}(\mathbf{x}) = \mathbf{0}$ and $k(\mathbf{x}) = 0$] is the *optimal FDSP* (oFDSP) generated by the *optimal OEEF* (oOEEF), and the corresponding BBP is the *optimal BBP* (oBBP). We label the oOEEF $\mathbf{e}^* = E\mathbf{e}_n^*$, and the oBBP by $(\mathbf{x}_{oBBP}, E_{oBBP})$. Thus, in the oBBP, the corresponding oOEEF, $\mathbf{e}_n^*$, takes the optimal intensity, $E = E_{oBBP}$, to transform the original potential, $V(\mathbf{x})$, into a perturbed potential, $V_{\mathbf{e}_n^*}(\mathbf{x}, E)$, exhibiting a shoulder around this point, $\mathbf{x} = \mathbf{x}_{oBBP}$: the barrier for this reaction valley has been annihilated.

Once the optimal conditions that an oFDSP should satisfy are known, we will now deal with the problem of finding the oBBP and optimal electric field, $(\mathbf{e}^*)$, since both will characterize the oFDSP curve and the oOEEF, $(\mathbf{e}_n^*)$. According to the previous discussion, the set of necessary and sufficient conditions that an oBBP should satisfy are given by Eqs. (17) and (19), with $\mathbf{k}(\mathbf{x}) = \mathbf{0}$ and $k(\mathbf{x}) = 0$. With these necessary and sufficient conditions, we have to find $M + 3$ equations, whose solutions give the M-unknowns, $\mathbf{x}_{oBBP}$ plus the three-unknowns related with the optimal electric field, now labeled $\mathbf{e}_{oBBP}^* = (\varepsilon_x^{*o}, \varepsilon_y^{*o}, \varepsilon_z^{*o}) = E_{oBBP}(e_x^*, e_y^*, e_z^*) = E_{oBBP}\mathbf{e}_n^*$. Let us stress that a basic condition should be fulfilled prior to finding the solutions of these equations: at the point $\mathbf{x}$ to be transformed into an oBBP on the effective (or perturbed) PES, the gradient vectors and the Hessian matrices of both functions, $V(\mathbf{x})$ and $P_{\mathbf{e}_n}(\mathbf{x}, E)$, must be different from the zero vectors and zero matrices, respectively.

Once the formal conditions defining the oBBP and oOEEF have been established, we describe the basic steps for its practical calculation:

1. *Location of $\mathbf{x}_{oBBP}$ associated with a given reaction valley on the PES.* $\mathbf{x}_{oBBP}$ is the point that satisfies Eq. (14), being a GE point with eigenvalue equal to zero. The location of this point is based on finding the point $\mathbf{x}$ where the so-called $\sigma(\mathbf{x})$-function, $\sigma(\mathbf{x}) = \mathbf{g}^T(\mathbf{x})\mathbf{H}^2(\mathbf{x})\mathbf{g}(\mathbf{x})/(\mathbf{g}^T(\mathbf{x})\mathbf{g}(\mathbf{x}))$, has value zero. The $\sigma(\mathbf{x})$-function was already introduced in Ref. 76 for finding the optimal mechanochemical pulling force. Practical schemes and algorithms for this purpose are described in Refs. 76 and 77. We note that the best starting point of these algorithms is the point with the higher square gradient norm of the Intrinsic Reaction Coordinate (IRC) path[79,80] located on the reaction valley of interest. The first and second derivatives with respect to $\mathbf{x}$ of $\{d_i(\mathbf{x})\}_{i=x,y,z}$ and $\{a_{ij}(\mathbf{x})\}_{i,j=x,y,z}$ should be computed at this point $\mathbf{x}$ and be sure that they are not simultaneously zero.
2. *Imposing the condition that $\mathbf{x}_{oBBP}$ point belongs to the oFDSP.* The $\mathbf{x}_{oBBP}$ point should belong to a FDSP curve, specifically the oFDSP. For this reason, Eq. (6) should be satisfied at this $\mathbf{x}_{oBBP}$ point. In order to impose this necessary condition of $\mathbf{x}_{oBBP}$, we multiply Eq. (6) from the left by the outer gradient projector,

$$\left(\mathbf{I} - \frac{\mathbf{g}(\mathbf{x}_{oBBP})\mathbf{g}^T(\mathbf{x}_{oBBP})}{\mathbf{g}^T(\mathbf{x}_{oBBP})\mathbf{g}(\mathbf{x}_{oBBP})}\right)\mathbf{m}_{\mathbf{e}_n^*}(\mathbf{x}_{oBBP}, E_{oBBP}) = \mathbf{0}. \tag{21}$$

Using Eqs. (3) and (5) and the recalling that $\mathbf{e} = E\mathbf{e}_n$, we rewrite the $\mathbf{m}_{\mathbf{e}_n}(\mathbf{x}, E)$ vector at the oBBP as

$$\begin{aligned}\mathbf{m}_{\mathbf{e}_n^*}(\mathbf{x}_{oBBP}, E_{oBBP}) &= -\Big\{[\nabla_{\mathbf{x}}\mathbf{d}^T(\mathbf{x}_{oBBP})] \\ &\quad + E_{oBBP}/2[\nabla_{\mathbf{x}}\mathbf{f}_{\mathbf{e}_n^*}^T(\mathbf{x}_{oBBP})]\Big\}\mathbf{e}_{oBBP}^* \\ &= -\mathbf{N}_{\mathbf{e}_n^*}(\mathbf{x}_{oBBP}, E_{oBBP})\mathbf{e}_{oBBP}^*. \end{aligned} \tag{22}$$

Substituting Eq. (22) into Eq. (21) and multiplying the resulting expression from the left by its transposed, one finds

$$\begin{aligned}&\mathbf{e}_{oBBP}^{*T}\mathbf{N}_{\mathbf{e}_n^*}^T(\mathbf{x}_{oBBP}, E_{oBBP})\left[\mathbf{I} - \frac{\mathbf{g}(\mathbf{x}_{oBBP})\mathbf{g}^T(\mathbf{x}_{oBBP})}{\mathbf{g}^T(\mathbf{x}_{oBBP})\mathbf{g}(\mathbf{x}_{oBBP})}\right] \\ &\quad\times \mathbf{N}_{\mathbf{e}_n^*}(\mathbf{x}_{oBBP}, E_{oBBP})\mathbf{e}_{oBBP}^* \\ &\quad = \mathbf{e}_{oBBP}^{*T}\mathbf{D}(\mathbf{x}_{oBBP}, \mathbf{e}_{oBBP}^*)\mathbf{e}_{oBBP}^* = 0. \end{aligned} \tag{23}$$

Thus, imposing the FDSP condition, we obtain the first equation, Eq. (23), that should be satisfied by the oOEEF. We note that the matrix $\mathbf{D}(\mathbf{x}_{oBBP}, \mathbf{e}_{oBBP}^*)$ has dimension 3×3 and that $\det[\mathbf{D}(\mathbf{x}_{oBBP}, \mathbf{e}_{oBBP}^*)] = 0$.
3. *The eigenvalue condition at $\mathbf{x}_{oBBP}$.* Equation (19b) should be satisfied at $\mathbf{x}_{oBBP}$ with $k(\mathbf{x}_{oBBP}) = 0$ since we are in a point of a GE curve that the eigenvalue of the gradient eigenvector is equal to zero. The eigenvalue condition, $\mathbf{g}^T(\mathbf{x}_{oBBP})\mathbf{H}(\mathbf{x}_{oBBP})\mathbf{g}(\mathbf{x}_{oBBP}) = 0$, is already satisfied from *item* (1); thus, we need to find an electric field, which makes the term $\mathbf{g}^T(\mathbf{x}_{oBBP})\mathbf{F}_{\mathbf{e}_n^*}(\mathbf{x}_{oBBP}, E_{oBBP})\mathbf{g}(\mathbf{x}_{oBBP})$ equal to zero. For this purpose, we take the expression of $k(\mathbf{x})$ evaluated at $\mathbf{x}_{oBBP}$,

$$\begin{aligned}k(\mathbf{x}_{oBBP}) &= \frac{\mathbf{g}^T(\mathbf{x}_{oBBP})\mathbf{F}_{\mathbf{e}_n^*}(\mathbf{x}_{oBBP}, E_{oBBP})\mathbf{g}(\mathbf{x}_{oBBP})}{\mathbf{g}^T(\mathbf{x}_{oBBP})\mathbf{g}(\mathbf{x}_{oBBP})} \\ &= \sum_{i=x,y,z}\varepsilon_i^{*o}\frac{\mathbf{g}^T(\mathbf{x}_{oBBP})\mathbf{M}_i(\mathbf{x}_{oBBP}, \mathbf{e}_{oBBP}^*)\mathbf{g}(\mathbf{x}_{oBBP})}{\mathbf{g}^T(\mathbf{x}_{oBBP})\mathbf{g}(\mathbf{x}_{oBBP})} \\ &= \sum_{i=x,y,z}\varepsilon_i^{*o}\frac{\mathbf{g}^T(\mathbf{x}_{oBBP})\mathbf{t}_i(\mathbf{x}_{oBBP}, \mathbf{e}_{oBBP}^*)}{\sqrt{\mathbf{g}^T(\mathbf{x}_{oBBP})\mathbf{g}(\mathbf{x}_{oBBP})}} \\ &= \sum_{i=x,y,z}\varepsilon_i^{*o}z_i(\mathbf{x}_{oBBP}, \mathbf{e}_{oBBP}^*) \\ &= \mathbf{e}_{oBBP}^{*T}\mathbf{z}(\mathbf{x}_{oBBP}, \mathbf{e}_{oBBP}^*) = 0. \end{aligned} \tag{24}$$

In the derivation of Eq. (24), we have used Eq. (11) and the following expression:

$$\frac{\mathbf{M}_i(\mathbf{x}_{oBBP},\mathbf{e}^*_{oBBP})\mathbf{g}(\mathbf{x}_{oBBP})}{\sqrt{\mathbf{g}^T(\mathbf{x}_{oBBP})\mathbf{g}(\mathbf{x}_{oBBP})}} = \mathbf{t}_i(\mathbf{x}_{oBBP},\mathbf{e}^*_{oBBP}). \quad (25)$$

We note that we use $\mathbf{z}$ for the scalar product in Eq. (24), being $\mathbf{z}(\mathbf{x}_{oBBP},\mathbf{e}^*_{oBBP})$ a vector of dimension three. Equation (24) gives the second expression that oOEEF should satisfy. Equation (24) can also be written as

$$\left(\mathbf{I} - \frac{\mathbf{z}(\mathbf{x}_{oBBP},\mathbf{e}^*_{oBBP})\mathbf{z}^T(\mathbf{x}_{oBBP},\mathbf{e}^*_{oBBP})}{\mathbf{z}^T(\mathbf{x}_{oBBP},\mathbf{e}^*_{oBBP})\mathbf{z}(\mathbf{x}_{oBBP},\mathbf{e}^*_{oBBP})}\right)\mathbf{e}^*_{oBBP} = \mathbf{P}^\perp_{\mathbf{z}}(\mathbf{x}_{oBBP},\mathbf{e}^*_{oBBP})\mathbf{e}^*_{oBBP} = \mathbf{e}^*_{oBBP}. \quad (26)$$

4. *The eigenvector condition* $\mathbf{k}(\mathbf{x}_{oBBP}) = \mathbf{0}$. At the $\mathbf{x}_{oBBP}$ point, Eq. (19a) should satisfy with $\mathbf{k}(\mathbf{x}_{oBBP}) = \mathbf{0}$ for either $\mathbf{H}(\mathbf{x}_{oBBP})$ and $\mathbf{F}_{\mathbf{e}^*_n}(\mathbf{x}_{oBBP}, E_{oBBP})$. For $\mathbf{H}(\mathbf{x}_{oBBP})$, this condition is already satisfied from *item* (1); thus, we need to find an electric field such that this condition is satisfied for $\mathbf{F}_{\mathbf{e}^*_n}(\mathbf{x}_{oBBP}, E_{oBBP})$. For this purpose, we take the definition of $\mathbf{k}(\mathbf{x})$ applied on the $\mathbf{F}_{\mathbf{e}_n}(\mathbf{x}, E)$ at the oBBP point, and from Eq. (24), $k(\mathbf{x}_{oBBP}) = 0$, we compute

$$\begin{aligned}\mathbf{k}^T(\mathbf{x}_{oBBP})\mathbf{k}(\mathbf{x}_{oBBP}) + k^2(\mathbf{x}_{oBBP}) &= \frac{\mathbf{g}^T(\mathbf{x}_{oBBP})\mathbf{F}^2_{\mathbf{e}^*_n}(\mathbf{x}_{oBBP}, E_{oBBP})\mathbf{g}(\mathbf{x}_{oBBP})}{\mathbf{g}^T(\mathbf{x}_{oBBP})\mathbf{g}(\mathbf{x}_{oBBP})} \\ &= \sum_{i=x,y,z}\sum_{j=x,y,z}\varepsilon^{*o}_i\varepsilon^{*o}_j\mathbf{t}^T_i(\mathbf{x}_{oBBP},\mathbf{e}^*_{oBBP}) \\ &\quad\times\mathbf{t}_j(\mathbf{x}_{oBBP},\mathbf{e}^*_{oBBP}) \\ &= \mathbf{e}^{*T}_{oBBP}\mathbf{T}(\mathbf{x}_{oBBP},\mathbf{e}^*_{oBBP})\mathbf{e}^*_{oBBP} = 0. \quad (27)\end{aligned}$$

Here, $\mathbf{T}(\mathbf{x}_{oBBP},\mathbf{e}^*_{oBBP})$ is a matrix of dimension 3×3, and it is positive definite. Equation (27) is the third and last condition that oOEEF should satisfy.

5. *Proposed algorithm to find* $\mathbf{e}^*_{oBBP}$. The basic flowchart for a practical implementation of the PMED model described in this work is represented in Fig. 1. For a given reaction valley of the PES, the main goals of this procedure consist in (i) locating the corresponding oBBP, (ii) calculating the oOEEF for this oBBP to annihilate the reaction barrier, and (iii) calculating the corresponding oFDSP curve to check that the process becomes barrierless under the action of the oOEEF. In the following, we refer to the corresponding parts of the flowchart to indicate the input and output data required to solve the equations at each step. The necessary and sufficient conditions to find the oBBP corresponding to previous steps 1 and 2 correspond to procedure ① in Fig. 1, whereas steps 3 and 4 provide the necessary and sufficient conditions of the corresponding optimal direction $\mathbf{e}^*_{oBBP}$ of the applied OEEF and its optimal intensity. An iterative procedure to do this search by solving the following equations by exploring different directions of the normalized vector field is as follows. The set of Eqs. (23), (26), and (27) gives necessary and sufficient conditions to find the $\mathbf{e}^*_{oBBP}$ vector. A way to solve this system of equations is first to substitute Eq. (26) into Eqs. (23) and (27) and next sum the resulting equations,

$$\begin{aligned}&\mathbf{e}^{*T}_{oBBP}\mathbf{P}^\perp_{\mathbf{z}}(\mathbf{x}_{oBBP},\mathbf{e}^*_{oBBP}) \\ &\quad\times[\mathbf{D}(\mathbf{x}_{oBBP},\mathbf{e}^*_{oBBP}) + \mathbf{T}(\mathbf{x}_{oBBP},\mathbf{e}^*_{oBBP})] \\ &\quad\times\mathbf{P}^\perp_{\mathbf{z}}(\mathbf{x}_{oBBP},\mathbf{e}^*_{oBBP})\mathbf{e}^*_{oBBP} = \mathbf{e}^{*T}_{oBBP} \\ &\quad\times\mathbf{G}(\mathbf{x}_{oBBP},\mathbf{e}^*_{oBBP})\mathbf{e}^*_{oBBP} = 0. \quad (28)\end{aligned}$$

From an inspection of Eq. (28), we can observe that $\det[\mathbf{G}(\mathbf{x}_{oBBP},\mathbf{e}^*_{oBBP})] = 0$. Let $\boldsymbol{\gamma}$ be the eigenvector with a null eigenvalue of the $\mathbf{G}(\mathbf{x}_{oBBP},\mathbf{e}^*_{oBBP})$ matrix; then,

$$\begin{aligned}&\boldsymbol{\gamma}^T\mathbf{P}^\perp_{\mathbf{z}}(\mathbf{x}_{oBBP},\mathbf{e}^*_{oBBP})\mathbf{D}(\mathbf{x}_{oBBP},\mathbf{e}^*_{oBBP}) \\ &\quad\times\mathbf{P}^\perp_{\mathbf{z}}(\mathbf{x}_{oBBP},\mathbf{e}^*_{oBBP})\boldsymbol{\gamma} \\ &\quad= -\boldsymbol{\gamma}^T\mathbf{P}^\perp_{\mathbf{z}}(\mathbf{x}_{oBBP},\mathbf{e}^*_{oBBP})\mathbf{T}(\mathbf{x}_{oBBP},\mathbf{e}^*_{oBBP}) \\ &\quad\times\mathbf{P}^\perp_{\mathbf{z}}(\mathbf{x}_{oBBP},\mathbf{e}^*_{oBBP})\boldsymbol{\gamma} = 0 \quad (29)\end{aligned}$$

since both matrices have zero as its lowest eigenvalue. At this point, it is important to consider that there is no reason why $\mathbf{z}^T(\mathbf{x}_{oBBP},\mathbf{e}^*_{oBBP})\boldsymbol{\gamma} = 0$ since

$$\begin{aligned}&\mathbf{z}^T(\mathbf{x}_{oBBP},\mathbf{e}^*_{oBBP})\mathbf{G}(\mathbf{x}_{oBBP},\mathbf{e}^*_{oBBP})\boldsymbol{\gamma} \\ &\quad= 0\cdot\mathbf{z}^T(\mathbf{x}_{oBBP},\mathbf{e}^*_{oBBP})\boldsymbol{\gamma}. \quad (30)\end{aligned}$$

For this reason, an Euler orthogonal transformation, $\mathbf{R}(\psi,\theta,\phi)$, is performed in such a way that $\mathbf{z}^T(\mathbf{x}_{oBBP},\mathbf{e}^*_{oBBP})\mathbf{R}(\psi,\theta,\phi)\boldsymbol{\gamma} = 0$. This rotated $\boldsymbol{\gamma}$ vector is taken as the $\mathbf{e}^*_n$-vector and satisfies Eq. (24). Note that this rotation makes invariant the trace of the $\mathbf{G}(\mathbf{x}_{oBBP},\mathbf{e}^*_{oBBP})$ matrix. Substituting this $\mathbf{e}^*_n$ vector in the expression

$$\begin{aligned}&\mathbf{m}^T_{\mathbf{e}^*_n}(\mathbf{x}_{oBBP}, E_{oBBP})\mathbf{m}_{\mathbf{e}^*_n}(\mathbf{x}_{oBBP}, E_{oBBP}) \\ &\quad-\mathbf{g}^T(\mathbf{x}_{oBBP})\mathbf{g}(\mathbf{x}_{oBBP}) = 1/4\mathbf{p}^T_{\mathbf{e}^*_n}(\mathbf{x}_{oBBP}) \\ &\quad\times\mathbf{p}_{\mathbf{e}^*_n}(\mathbf{x}_{oBBP})E^4_{oBBP} + \mathbf{h}^T_{\mathbf{e}^*_n}(\mathbf{x}_{oBBP})\mathbf{p}_{\mathbf{e}^*_n}(\mathbf{x}_{oBBP}) \\ &\quad\times E^3_{oBBP} + \mathbf{h}^T_{\mathbf{e}^*_n}(\mathbf{x}_{oBBP})\mathbf{h}_{\mathbf{e}^*_n}(\mathbf{x}_{oBBP})E^2_{oBBP} \\ &\quad-\mathbf{g}^T(\mathbf{x}_{oBBP})\mathbf{g}(\mathbf{x}_{oBBP}) = 0 \quad (31)\end{aligned}$$

by solving this quartic polynomial form on E_{oBBP}, we obtain E_{oBBP} and from this $\mathbf{e}^*_{oBBP}$ vector. Equation (31) is derived using Eqs. (6) and (7). The process is repeated by substituting the current $\mathbf{e}^*_{oBBP}$ vector into the $\mathbf{G}(\mathbf{x}_{oBBP},\mathbf{e}^*_{oBBP})$ matrix until the new and previous $\mathbf{e}^*_{oBBP}$ vectors do not change within some criterium. At the initial step, the matrix $\mathbf{G}(\mathbf{x}_{oBBP},\mathbf{0})$ is taken.

6. *Selection of the optimal OEEF.* From the whole set of solutions, we take the one that lowers the value of the

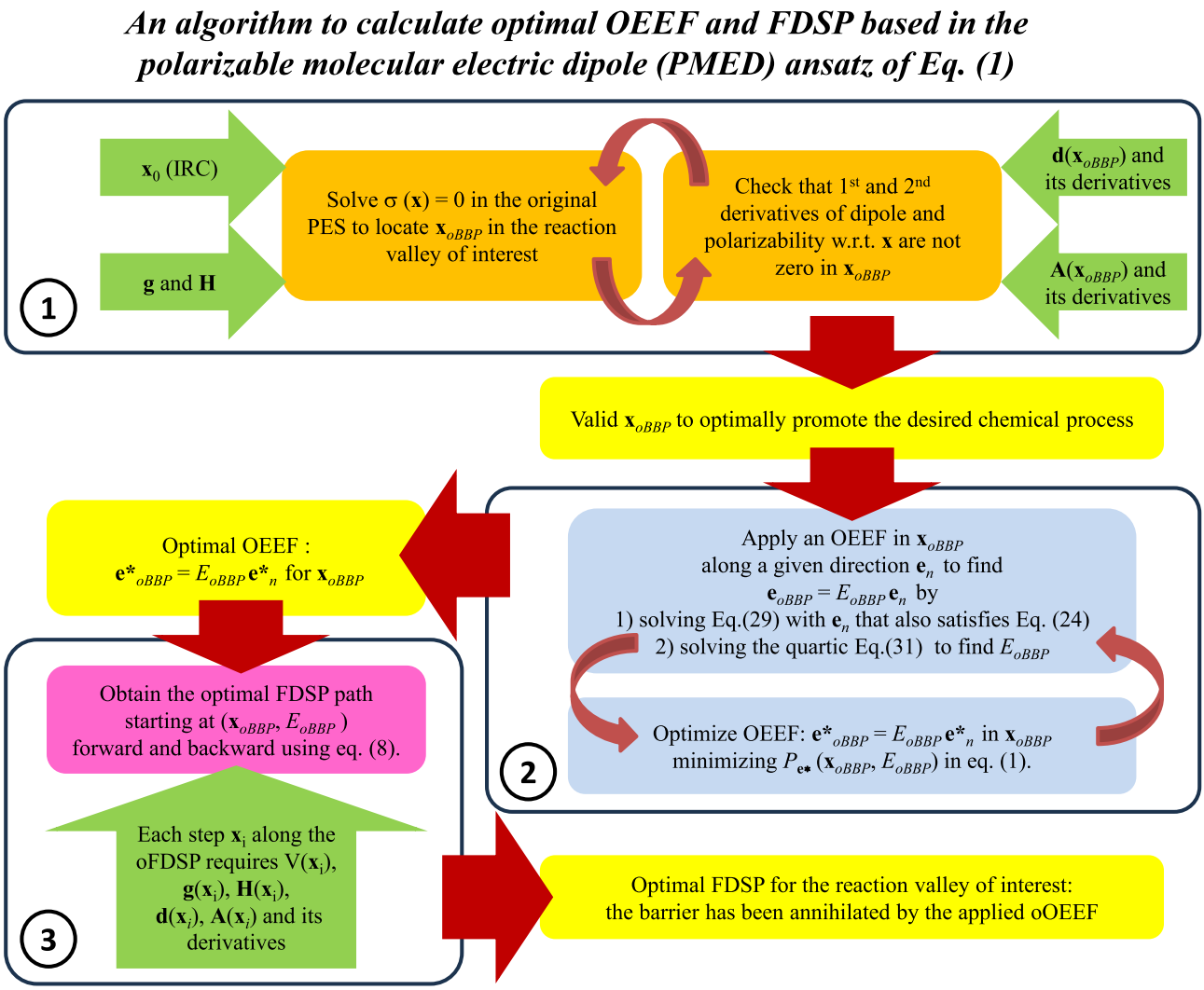

FIG. 1. Flow chart describing the proposed PMED algorithm to calculate the oBBP (step 1), oOEEF (step 2), and oFSDP (step 3) for the reaction valley of interest on the PES. Color code: the required input data from a standard molecular electronic structure code are marked in green; the procedure to locate the oBBP (a catastrophe point in the original PES) using the algorithm described in Refs. 76 and 77 is marked in orange; the procedure to calculate the optimal OEEF at $\mathbf{x}_{oBBP}$ is marked in blue; and the procedure to calculate the optimal FDSP passing through $\mathbf{x}_{oBBP}$ is marked in pink.

perturbed function, namely, $P_{\mathbf{e}_n^*}(\mathbf{x}_{oBBP}, E_{oBBP}) = -\mathbf{d}^T(\mathbf{x}_{oBBP}) \times \mathbf{e}^*_{oBBP} - 1/2\mathbf{e}^{*T}_{oBBP}\mathbf{A}(\mathbf{x}_{oBBP})\mathbf{e}^*_{oBBP}$, already defined in Eq. (1). In this way, we take the solution that minimizes the barrier of the original PES, $V(\mathbf{x})$, as much as possible. Once the solution is taken, $\mathbf{e}^*_{oBBP}$, we normalize it obtaining E_{oBBP} and the normalized direction $\mathbf{e}^*_n$. With this normalized direction, the integration of the oFDSP path is carried out, starting at the oBBP point, $(\mathbf{x}_{oBBP}, E_{oBBP})$, forward and backward using Eq. (8). This searching scheme of the oOEEF in the oBBP point of the unperturbed PES corresponds to procedure ② in Fig. 1 and only requires the information of the oBBP structure [$\mathbf{x}$ coordinates, the energy $V(\mathbf{x})$, gradient $\mathbf{g}(\mathbf{x})$ and hessian $\mathbf{H}(\mathbf{x})$, electric dipole moment $\mathbf{d}(\mathbf{x})$ and its derivatives, and electric polarizability tensor $\mathbf{A}(\mathbf{x})$ and its derivatives] provided by standard electronic structure codes; hence, it is simple and computationally efficient. However, the integration of the oFSDP curve implied by procedure ③ in Fig. 1 is more computationally demanding since this information is required for each step of integration. However, knowing the oOEEF field $\mathbf{e}^*_{oBBP} = E_{oBBP}\mathbf{e}^*_n$, starting at the oBBP point with the optimal direction of the electric field is usually enough to understand and interpret the most efficient way to reduce the reaction barrier for this reaction valley of the PES.

This is the essential structure of the PMED model and algorithm, which transforms a GE point of the original PES with the eigenvalue equal to zero (i.e., a point where $\det[\mathbf{H}(\mathbf{x})] = 0$) into an oBBP

point of the perturbed PES where $\det\left[\mathbf{H}_{\epsilon_n^*}\left(\mathbf{x}_{oBBP}, E_{oBBP}\right)\right] = 0$. This is the essential structure to understand and control electrostatic catalytic effects by applying an OEEF. However, it is important to stress the fact that other special points of the original PES with interesting topological properties can also be transformed into a BBP of the perturbed PES, being one of them the valley-ridged-inflection point (VRI).[81–84] The modification of the PMED algorithm to the case of VRI points and other non-stationary points is given in Appendix A and is applied to a toy model system in Appendix B.

III. APPLICATION OF THE PMED MODEL TO CHEMICAL SYSTEMS

In this section, we expose the behavior of the present PMED model in two chemical examples. The calculations were made with the ORCA 5.0.3[85–89] suite of programs. The data generated by this program [for the required input data for each $\mathbf{x}$ structure, the energy $V(\mathbf{x})$, gradient $\mathbf{g}(\mathbf{x})$ and hessian $\mathbf{H}(\mathbf{x})$, electric dipole moment $\mathbf{d}(\mathbf{x})$, and electric polarizability tensor $\mathbf{A}(\mathbf{x})$] are used by MANULS program,[90] an open-source Python software package where the PMED algorithm described in Subsection II B is implemented. The first and second derivatives of the energy, dipole, and polarizability for reduced spaces are calculated numerically in the MANULS code with a central differences approach. This package is available in https://github.com/MSeveri96/MANULS.[90] Additionally, the exact version of MANULS used to run these calculations is available from Severi.[91]

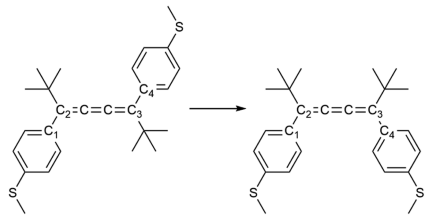

FIG. 2. The *trans*-to-*cis* (or *E*-to-*Z*) isomerization of [3]cumulene derivative (*E*)-((2,2,7,7-tetramethylocta-3,4,5-triene-3,6-diyl)bis(4,1-phenylene))bis(methylsulfane) studied. The atom numbering used to define the central dihedral angle is indicated.

A. The *trans*-to-*cis* isomerization of a [3]cumulene derivative

The aim of this example is to show how the optimal external electric field annihilates the energy barrier of a *trans*-to-*cis* isomerization of a [3]cumulene derivative, taking into account the electric polarizability effects. We have chosen this chemical process because recent experiments[13] have shown that the OEEFs accelerate isomerizations in these types of systems. A representation of the molecular process studied is shown in Fig. 2. We start by calculating the potential energy curve that describes the isomerization. To do so, we performed constrained geometry optimizations in which the dihedral angle described by the C1–C2–C3–C4 atoms is fixed and the remaining degrees of freedom are optimized (see Fig. 2 for the atom numbering). We scanned the dihedral from 0° to 180° with a step of 5°. By convention, the s-cis isomer is described by a 0° dihedral angle, while the s-trans is described by a 180° dihedral angle.

The calculations employed the UHF[92,93] method and the $6-31G^*$ basis set[94] *in vacuo*. The computational approach relied on the broken-symmetry formalism. In this case, we calculated the natural orbitals associated with the lowest triplet state and used them as a guess to perform the calculations on the singlet state since it shows a significant open shell/diradical character around the TS structure.[95] The calculations were made with the ORCA 5.0.3[85–89] suite of programs.

1. Results and discussion

The molecular geometries of the *trans* isomer, the *cis* isomer, and the transition state for the conversion process of the [3]cumulene derivative are shown in Figs. 3(a)–3(c), respectively. The molecular geometry of the oBBP is shown in Fig. 4 along with the direction of the optimal OEEF using the PMED model and the simplified version considering the electric dipole moment only. Finally, the unperturbed PES and the surfaces perturbed by the optimal OEEF (i.e., the oOEEF) using the PMED model and the simplified version of the model are shown in Fig. 5. The optimal bond-breaking point corresponds to a dihedral angle equal to 140°. Note that the oBBP structure is an intrinsic property of the unperturbed PES. In this point, the optimal OEEF calculated considering both the electric dipole moment and polarizability is in the $(-0.459, 0.487, 0.743)$ direction and its intensity is 0.0086 a.u. = 0.442 V/Å. The optimal external electric field calculated considering only the electric dipole moment is in the $(-0.808, 0.273, 0.522)$ direction, and its intensity is

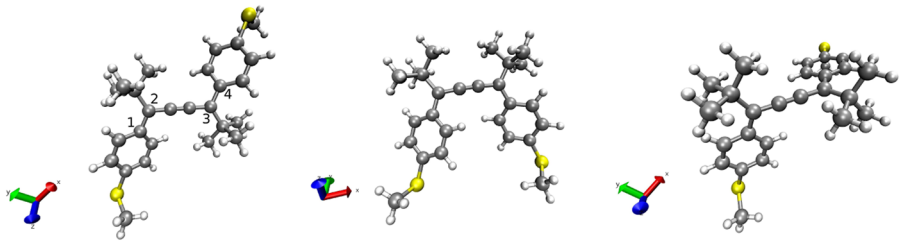

(a) *trans isomer* (b) *cis isomer* (c) *transition state*

FIG. 3. Representation of the structure of the stationary points of the potential energy curve for the *trans*-to-*cis* isomerization process of the [3]cumulene derivative.

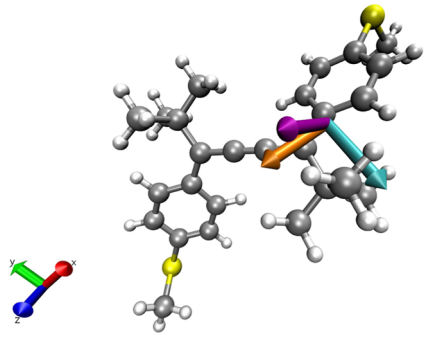

FIG. 4. Molecular geometry of the optimal bond-breaking point, oBBP, for the *trans*-to-*cis* isomerization process of the [3]cumulene derivative. Purple arrow: direction of the optimal external electric field calculated considering the polarizability and the dipole. Orange arrow: direction of the optimal external electric field calculated considering only the dipole. Cyan arrow: direction of the molecular electric dipole moment vector.

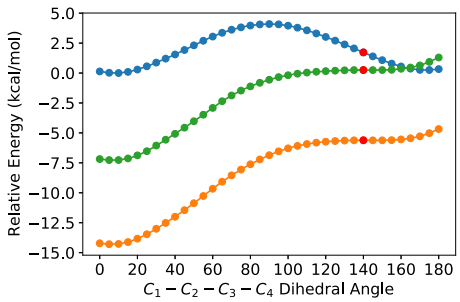

FIG. 5. Curves on the PES describing the *trans*-to-*cis* isomerization of the [3]cumulene derivative in all the three discussed cases: no OEEF applied (unperturbed PES) in blue; perturbed PES with optimal OEEF calculated considering the PMED model in orange; and perturbed PES with optimal OEEF calculated considering a simplified model considering only the electric dipole moment in green. The energy values are relative to the energy minimum of the PES calculated without the effect of the electric field, that is, the *cis* isomer in the gas phase. The red dots represent the location of the optimal bond breaking point.

0.0091 a.u. = 0.470 V/Å. The angle between the fields calculated in the two approximations is 26.9°, showing the important effect of the polarizability of the molecular charge distribution in response to the applied oOEEF. Here, it is worth to mention that we have recomputed the stationary points of the PES of the cumulene system at the B3LYP-D3BJ/6-31G* level. With this approach, the *cis*-to-TS barrier and the *trans*-to-TS barriers are ~25 kcal/mol, a higher value than that obtained at the UHF level (~5 kcal/mol), which is in line with the results reported in Ref. 96. Therefore, the barrier obtained at the UHF level is most likely smaller than the real barrier, which means that our predicted field strength for the annihilation of the barrier is likely smaller than the real one.

A comparison of the original and the perturbed PES in Fig. 5 clearly shows the essential role of the oBBP in rationalizing the effect of the applied oOEEF on the system and the fact that the TS has a minor role to understand the thermodynamic properties of the unperturbed PES. In addition, it clearly shows the fact that application of an oOEEF has a global effect on the PES, which is usually ignored in simplified models based on the unperturbed PES.

B. The 1,3-dipolar cycloaddition of fulminic acid plus acetylene to isoxazole

As a second realistic chemical example, we will focus on one reaction that belongs to the family of the 1,3-dipolar cycloadditions, which constitutes an important class of pericyclic rearrangements. In particular, we will study the Huisgen reaction, which is an example of exergonic fusion process where two unsaturated reactants come together to form five-membered heterocycles. The Huisgen reaction between fulminic acid and acetylene to form isoxazole has already been studied computationally using a variety of energy functionals and basis sets. The rather low energy barriers reported in previous computational studies for this reaction are consistent with the experimental observation that 1,3-dipolar cycloadditions usually proceed under mild thermal conditions. Here, we study the cycloaddition reaction, and we will focus our efforts on finding the *optimal OEEF* that triggers the exothermic cycloaddition of fulminic acid and acetylene to isoxazole through a barrierless process.

All the calculations regarding the characterization of the PES and the scans were performed with the ORCA 5.0.3[85–89,97] suite of programs. The calculations are performed using the B3LYP functional[98–101] and def2-TZVP basis set *in vacuo*.[102] Every calculation employs the D3BJ dispersion correction[103,104] and the RIJCOSX approximation[97] (that is, the default in the ORCA code for DFT calculations).

The PES calculations were carried out using the following computational strategy: after the optimization of the reactants, the TS, and the product, three surface scans were performed by fixing two distances and optimizing the remaining coordinates. The first one consists in a surface scan fixing the C_1–C_2 and C_3–O bonds from 3.4 to 1.2 Å with a step of 0.1 Å. The second one consists in a surface scan fixing the C_1–C_2 and C_3–O bonds from 3.0 to 2.4 Å with a step of 0.025 Å. Finally, the third one consists in a surface scan fixing the C_1–C_2 and C_3–O bonds from 3.0 to 2.1 Å with a step of 0.04 Å, used only for the calculation of the FDSP path. The Huisgen reaction and the atom numbering are shown in Fig. 6. In addition to the energy value at each point of the grid, the permanent dipole moment (i.e., the dipole moment at zero field) and the polarizability were also computed at each point of the two-dimensional PES.

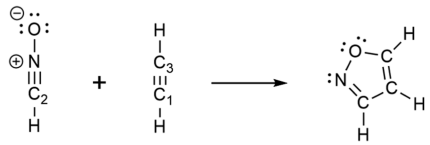

FIG. 6. The Huisgen reaction between fulminic acid plus acetylene to give isoxazole. The atom numbering is also reported.

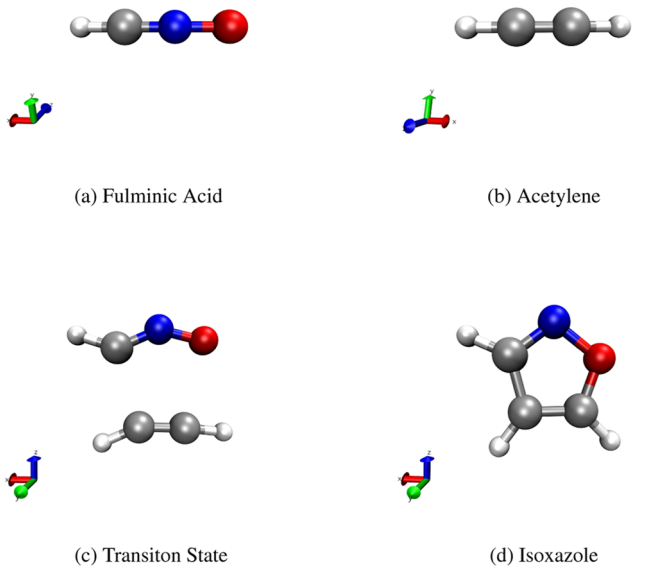

FIG. 7. Representation of (a) and (b) the reactants, (c) the transition state, and (d) the product of the 1–3 cycloaddition of fulminic acid and acetylene to isoxazole. The C_1–C_2 and C_3–O bond distances are 2.17 and 2.38 Å for TS and 1.42 and 1.34 Å for isoxazole.

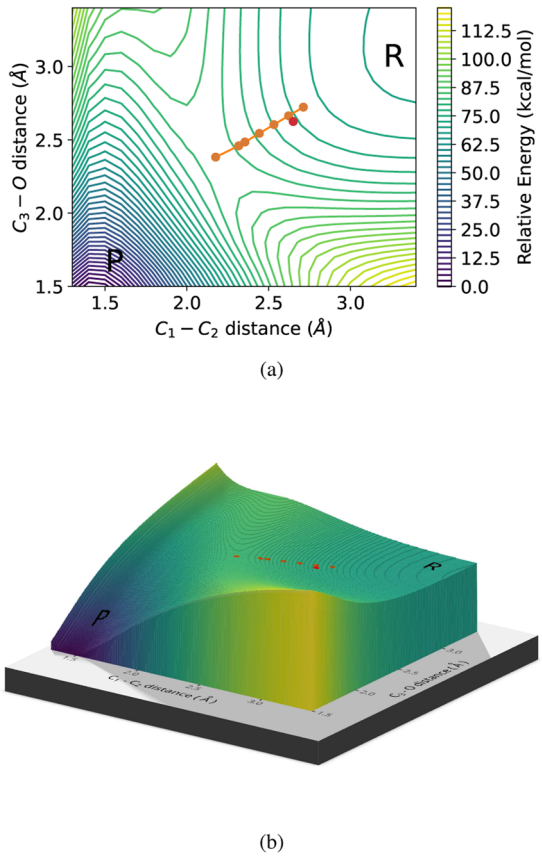

FIG. 8. 2D (a) and 3D (b) representations of the original (or unperturbed) PES for the Huisgen cycloaddition reaction in the space represented by the C_1–C_2 and C_3–O bond distances. The red dots represent the optimal BBP. The orange dots represent the IRC trajectory. The energy is relative to the products [the minimum of the surface on the bottom left of (a)]. R and P mark the reactants and products configurations, respectively.

1. Results and discussion

We first located the stationary points associated with the reactants and transition state configurations. The geometry of the minima and TS structures are shown in Fig. 7. The most important geometrical changes of the molecular system during the reaction process occur in the C_1–C_2 and C_3–O bond distances. This means that the reaction can be properly described in the subspace defined by these two coordinates. Taking this into account, we will find the *oBBP* for the cycloaddition of fulminic acid plus acetylene to isoxazole in the subspace defined by these two coordinates. Working in this two-dimensional subspace will also allow us to better illustrate the algorithm introduced in Subsection II B.

The original or unperturbed $V(\mathbf{x})$ PES in the two-dimensional subspace was computed by means of a set of constrained optimizations in which the values of the C_1–C_2 and C_3–O bond distances were fixed at given values reported in Subsection III B.

The *oBBP* of the cycloaddition reaction was located according to the algorithm described in Ref. 76, or that is the same to find the point of the GE curve where the eigenvalue of the gradient eigenvector of the Hessian matrix is near zero within some criterium. The unperturbed PES is reported in Fig. 8, along with the IRC starting from the TS and the oBBP. The red bold circle shown on the unperturbed PES of Fig. 8 marks the location of *oBBP* point, $(\mathbf{x}_{oBBP})$, being near to the IRC curve. Note the large difference between oBBP and TS structures and the fact that is sitting half way between TS and reactants. Now, we can compute the *oOEEF*, namely, $\mathbf{e}^*_{oBBP} = E_{oBBP}\mathbf{e}^*_n$ at the oBBP and the *oFDSP* curve using the normalized direction of *oOEEF* starting at the $\mathbf{x}_{oBBP}$ point. At this point, it is interesting to compute the oOEEF with the simplified model that only takes into account the electric dipole moment to assess the role of the polarizability in the determination of the oOEEF. The application of the PMED model including the polarizability of the electric dipole leads to an oOEEF in the $(-0.871, 0.036, -0.489)$ direction with 0.0879 a.u. = 4.52 V/Å intensity, whereas the simplified model leads to a different oOEEF pointing in the $(-0.722, +0.666, -0.188)$ direction with an intensity of 0.1937 a.u. = 9.96 V/Å. A representation of the oOEEFs is in Fig. 9, showing a large difference in direction and intensity when polarizability is taken into account. Indeed, while the oOEEFs obtained with both levels of approximation are successful in eliminating the reaction barrier (see Figs. 10 and 11), they differ considerably. The annihilation of the reaction barrier by the oOEEF is shown in Fig. 12 by comparing the energy profiles of the three paths (the IRC and the oFSDP provided by the two models) using the same energy scale. However, the differences of the corresponding oOEEFs show the importance of taking into account the polarization on the molecular charge distribution considered in the PMED model. In this case, the intensities (or strengths) of the oOEEFs computed with the two levels of approximation differ in

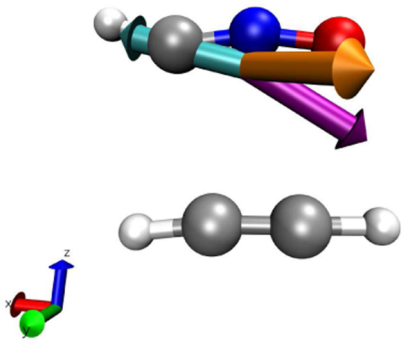

(a)

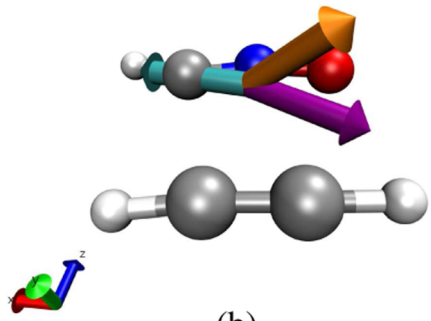

(b)

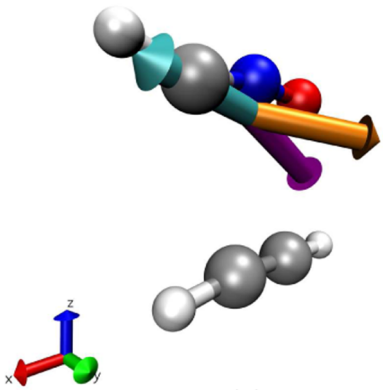

(c)

FIG. 9. (a)–(c) Three views from different perspectives of the oBBP geometry for the Huisgen cycloaddition reaction. The purple arrow represents the direction of the optimal external field calculated considering the PMED model (i.e., considering both the molecular electric polarizability and the dipole). The purple arrow represents the direction of the optimal external field calculated considering only the electric dipole. The cyan arrow represents the direction of the electric dipole moment vector.

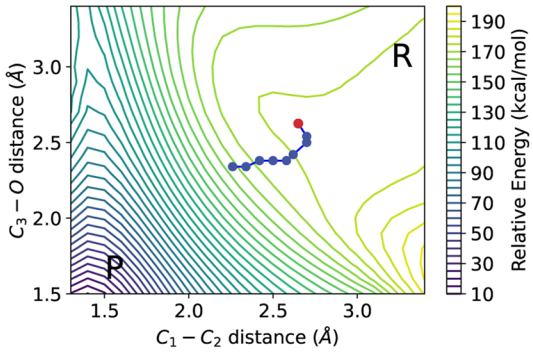

(a)

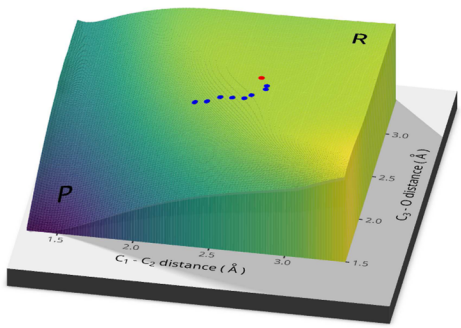

(b)

FIG. 10. 2D (a) and 3D (b) representations of the perturbed PES with an oOEEF calculated using the PMED model (i.e., by considering both the polarizability and the dipole) for the Huisgen cycloaddition reaction. The red dots represent the oBBP. The blue dots represent some calculated points of the oFDSP curve. The energy is relative to the product minimum configuration of the unperturbed PES in Fig. 8.

73% and the angle between the two field directions is even larger than in the cumulenic system, 44.7°, showing the essential contribution of the polarizability in reducing the oOEEF strength. The comparison of the oFSDP curves using the PMED model appears smoother than the corresponding curve from the simplified model, in line with the simultaneous breaking of the C_1–C_2 and C_3–O bonds expected for this kind of concerted cycloaddition. It should be mentioned that these electric field strengths required to annihilate the reaction barrier are larger than the strengths that can be exerted by STM and those fields predicted to exist in active sites of enzymes. In fact, for a molecular system under such strong electric fields, other effects beyond charge polarization would lead to different reaction mechanisms, including redox or charge transfer processes. This situation is clearly beyond the assumption of the pro-

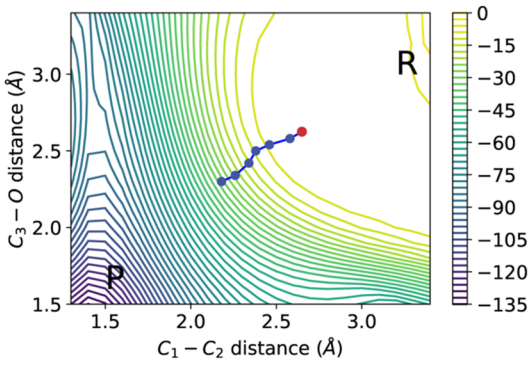

(a)

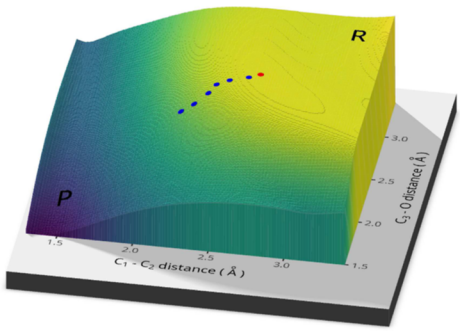

(b)

FIG. 11. 2D (a) and 3D (b) representations of the perturbed PES with an oOEEF calculated using the simplified model considering only the electric dipole for the Huisgen cycloaddition reaction. The red dots represent the oBBP. The blue dots represent some calculated points of the oFDSP curve. The energy is relative to the product minimum configuration of the unperturbed PES in Fig. 8.

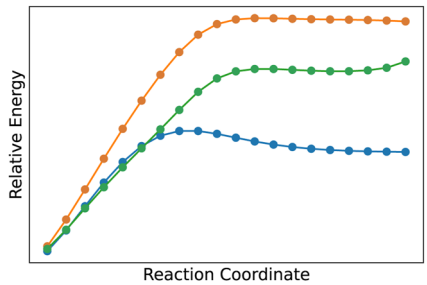

FIG. 12. Qualitative reaction profiles on the PES describing the Huisgen cycloaddition reaction in all the three discussed cases: no OEEF applied (unperturbed PES) in blue; perturbed PES with optimal OEEF calculated considering the PMED model in green; and perturbed PES with optimal OEEF calculated considering the simplified model considering only the electric dipole moment in orange.

posed PMED model acting on charge distributions defined by the wavefunction of each structure on the unperturbed PES. However, the important information provided by the PMED is the direction of the oOEEF, which, even for lower strengths, would lead to significant catalytic effects by substantially lowering the corresponding reaction barrier.

IV. CONCLUSIONS

In this article, we present a novel theoretical model based on the polarizable molecular electric dipole (PMED) ansatz, which is aimed at providing new tools to establish which is the optimal direction in which an external electric field should be applied to annihilate a given reaction barrier in the most efficient form. Here, we propose the PMED model, which is based on catastrophe and optimal control theories where the electric field enters in a quadratic way since we consider the electric dipole and polarizability to account for the response of the molecular system to an applied OEEF. The foundations of these theories have been presented previously in the context of mechanochemistry[76,77] and OEEF-driven chemical reactivity,[59,60] and its generalization in several ways is presented in this work. The most important generalization consists of the PMED model, which fully takes into account electric-field induced distortions of the molecular charge distribution taking into account the electric polarizability, thus going beyond simple treatments that rely exclusively on the intrinsic dipole moments of the stationary points (TS and reactants) of the unperturbed PES. Our previously proposed scheme based on a molecular electric dipole[59,60] is a significant improvement over these simplified "rigid" models, but the inclusion of the electric polarizability in the PMED model introduces the essential electrostatic response of the molecular system that can be treated in a feasible computational application due to the intractable complexity of the equations and its computational cost. The concept of barrier breakdown or bond-breaking points, *BBPs*, of the perturbed PES is central in our model due to their unique topological properties. These points embody essential topological information of the evolution of the perturbed (or effective) PES as a function of the direction and strength of the applied OEEF.

In the PMED model, for each direction of the OEEF (given by e_n) applied to promote a process along a given reaction valley of the unperturbed PES, there exists a BBP configuration lying somewhere between the reactants and the TS configurations of this reaction valley. Each BBP is a catastrophe point in which the reactants and the TS configurations coalesce in the perturbed PES for a given strength of the electric field parallel direction e_n. Once a BBP has been located, the evolution of the PES with the field strength (for a fixed direction e_n) can be obtained by the integration of the so-called FDSP curve. Within the manifold of BBPs associated with this reaction valley, there exists one configuration, so-called optimal BBP (oBBP), which is associated with the optimal OEEF (oOEEF) that corresponds to the minimum possible field strength to make the process barrierless.

The necessary and sufficient conditions to find the oBBP and its associated oOEEF are provided in this work, along with an efficient algorithm to evaluate them using the unperturbed PES only. After locating the oBBP using the algorithms presented in Refs. 77 and 76, the oOEEF can be found in a one-step procedure by imposing the two following conditions: (i) the Hessian of the original PES must

be equal to that of the perturbation coincide with those of the perturbation function at the oBBP configuration and (ii) each gradient is an eigenvector of the corresponding Hessian (gradient extremal condition). The PMED model has also been extended to other special points of the PES, such as the valley-ridged-inflection (VRI).[81–84] In addition, an algorithm is proposed and tested in a model 2D PES. The VRI points also have special topological properties that can be important for the description of the dynamics of chaotic systems under the influence of an OEEF.

The proposed PMED algorithm performs the calculation of the oBBP and the oOEEF in a two-step procedure that essentially requires the information related to the oBBP structure (gradient, hessian, electric dipole, and polarizability and their first and second derivatives), whereas the most computational demanding step is the integration of the oFSDP curve, which requires this information for each step of the integration. The algorithm has been implemented in an open-source Python software package[90] that can be interfaced with standard electronic structure packages.

The PMED model has been applied to describe the catalytic effects when OEEFs are applied to several model PESs and two relevant chemical reactions to show its capabilities and performance of the proposed algorithm. It should be mentioned that in some cases, the electric field strengths required to annihilate the reaction barrier can be significantly larger than those used in STM or the electric fields predicted to exist in active sites of enzymes. Under these conditions, other effects beyond charge polarization might take place (i.e., redox or charge transfer processes) and are beyond the PMED model. Nevertheless, the direction of the oOEEF still provides a relevant information since applied OEEFs with lower strengths would lead to significant catalytic effects by substantially lowering the corresponding reaction barrier. On the other hand, a generalization of the model to account for more realistic heterogeneous electric fields is likely possible, but this is a difficult endeavor since the model may likely result in very complex variational control equations when introducing complicated functions describing the position-dependence of the electric field. In future works, we will attempt to generalize the present model to account for simple forms of inhomogeneities of applied electric fields in STM junctions or in active sites of enzymes.

The chemical examples described in this work provide an interesting picture to explain electrostatic catalytic effects in molecular systems: for a given reaction valley, the effect of applying an electric field parallel to the direction dictated by the oOEEF with an increasing strength will distort the original PES in a way that the structure of the reactants' configuration will move closer to the TS configuration in the perturbed PES. For a sufficiently high intensity of the OEEF (the E_{oOEEF}), the reactants and TS configurations will coalesce at the optimal BBP, and then, the chemical process becomes barrierless. This image of both the reactants and TS configurations moving closer to each other on the perturbed PES and eventually coalescing at the oBBP as a result of the applied external field dictated by the oEEF provides a firm conceptual framework for the burgeoning field of electrostatic catalytic effects observed in different organic and biologic processes. In particular, the concept of oBBP can provide fundamental information to understand the mechanisms involved in enzymatic catalysis in view of the key role played by the electrostatic fields exerted by the active sites of enzymes in their catalytic activity. Finally, these examples show the central role played by the oBBP to understand this kind of chemical control and the fundamental implications of the catastrophe and control theories in chemistry.

ACKNOWLEDGMENTS

The authors acknowledge the financial support from the Spanish Ministerio de Economía y Competitividad, Project Nos. PID2019-109518GB-I00, PID2020-117803GB-I00, and CTQ2017-87773-P/AEI/FEDER, and Spanish Structures of Excellence María de Maeztu program through Grant No. CEX2021-001202-M. This work was supported by Agència de Gestió d'Ajuts Universitaris i de Recerca of Generalitat de Catalunya, Project No. Projecte 2021 SGR 00354. They also acknowledge the CINECA award under the ISCRA initiative for the availability of high-performance computing resources and support.

AUTHOR DECLARATIONS

Conflict of Interest

The authors have no conflicts to disclose.

Author Contributions

Josep Maria Bofill: Conceptualization (equal); Data curation (equal); Formal analysis (equal); Funding acquisition (equal); Investigation (equal); Methodology (equal); Project administration (equal); Resources (equal); Software (equal); Supervision (equal); Validation (equal); Visualization (equal); Writing – original draft (equal); Writing – review & editing (equal). **Marco Severi**: Conceptualization (equal); Data curation (lead); Formal analysis (equal); Funding acquisition (equal); Investigation (equal); Methodology (equal); Resources (equal); Software (lead); Validation (equal); Visualization (lead); Writing – original draft (lead); Writing – review & editing (lead). **Wolfgang Quapp**: Conceptualization (equal); Data curation (equal); Formal analysis (equal); Investigation (equal); Methodology (equal); Supervision (equal); Validation (equal); Visualization (equal); Writing – original draft (equal); Writing – review & editing (equal). **Jordi Ribas-Ariño**: Conceptualization (equal); Data curation (equal); Formal analysis (equal); Investigation (equal); Methodology (equal); Resources (equal); Supervision (equal); Validation (equal); Writing – original draft (lead); Writing – review & editing (lead). **Ibério de P. R. Moreira**: Conceptualization (equal); Data curation (supporting); Formal analysis (supporting); Funding acquisition (lead); Investigation (equal); Methodology (equal); Project administration (equal); Resources (equal); Supervision (equal); Validation (supporting); Visualization (equal); Writing – original draft (lead); Writing – review & editing (lead). **Guillermo Albareda**: Conceptualization (equal); Data curation (equal); Formal analysis (equal); Funding acquisition (equal); Investigation (equal); Methodology (equal); Supervision (equal); Validation (equal); Visualization (equal); Writing – original draft (equal); Writing – review & editing (equal).

DATA AVAILABILITY

The data that support the findings of this study are available from the corresponding author upon reasonable request.

APPENDIX A: GENERALIZATION OF THE PMED ALGORITHM DESCRIBED IN SEC. II B APPLIED TO OTHER SPECIAL POINTS OF THE PES

The algorithm described in Subsection II B shows how the OEEF transforms a GE point with the eigenvalue equal to zero of the original PES, a point where $\det[\mathbf{H}(\mathbf{x})] = 0$, into an oBBP point of the perturbed PES where $\det[\mathbf{H}_{\mathbf{e}_n^*}(\mathbf{x}_{oBBP}, E_{oBBP})] = 0$, but other points of the original PES can also be transformed to BBP of the perturbed PES, being one of them the valley-ridged-inflection (VRI) point.[81–84]

In fact, in a previous study, we already demonstrated that mechanical forces can transform a VRI point into a BBP.[61] We recall that a VRI point is also a GE point where normally the eigenvalue is not equal to zero[75] and thus does not satisfy the optimality conditions just described above. Here, we develop a formal scheme, similar to the one previously shown for the oBBP, to establish the necessary and sufficient conditions to locate the optimal VRI and OEEF by means of the topological properties of the VRI points on the unperturbed PES. Note that for a PES of more than two dimensions, VRIs are usually not isolated, single points (such as minima and SPs), but they exist as a manifold of points.[82–84,105–112] The VRI point transformed into a BBP will be labeled $\mathbf{x}_{vBBP}$. The algorithm to make this transformation is analogous to the PMED algorithm for locating oBBPs but with the following changes.

1. *Location of* $\mathbf{x}_{vBBP}$. An algorithm to locate a VRI point on the original PES, $V(\mathbf{x})$, is already described in Ref. 83. This point satisfies the eigenvalue equation $\mathbf{H}(\mathbf{x}_{vBBP})\mathbf{g}(\mathbf{x}_{vBBP}) = g(\mathbf{x}_{vBBP})\mathbf{g}(\mathbf{x}_{vBBP})$, being $g(\mathbf{x}_{vBBP})$ the eigenvalue normally different to zero. The VRI also satisfies the $\det[\mathbf{H}(\mathbf{x}_{vBBP})] = 0$ condition since another eigenvector of the $\mathbf{H}(\mathbf{x}_{vBBP})$ matrix has null eigenvalue. It should be verified that the first and second derivatives with respect to $\mathbf{x}$ of $\{d_i(\mathbf{x})\}_{i=x,y,z}$ and $\{a_{ij}(\mathbf{x})\}_{i,j=x,y,z}$ at $\mathbf{x}_{vBBP}$ are not simultaneously zero.
2. *Imposing the condition that the* $\mathbf{x}_{vBBP}$ *point belongs to the FDSP.* This step is similar to *item* (2) of the previous algorithm by changing $\mathbf{x}_{oBBP}$ by $\mathbf{x}_{vBBP}$.
3. *The eigenvalue condition at* $\mathbf{x}_{vBBP}$. At $\mathbf{x}_{vBBP}$, Eq. (19b) should be satisfied with $k(\mathbf{x}_{vBBP}) = g(\mathbf{x}_{vBBP})$ since we are in a point of the GE curve that the eigenvalue of the gradient eigenvector is equal to $g(\mathbf{x}_{vBBP})$. Thus, Eq. (24) now is

$$k(\mathbf{x}_{vBBP}) = \mathbf{e}_{vBBP}^T \mathbf{z}(\mathbf{x}_{vBBP}, \mathbf{e}_{vBBP}) = g(\mathbf{x}_{vBBP}). \tag{A1}$$

4. *The eigenvector condition* $\mathbf{k}(\mathbf{x}_{vBBP}) = \mathbf{0}$. At the $\mathbf{x}_{vBBP}$ point, Eq. (19a) is satisfied with $\mathbf{k}(\mathbf{x}_{vBBP}) = \mathbf{0}$. In this case, Eq. (27) now is

$$\mathbf{k}^T(\mathbf{x}_{vBBP})\mathbf{k}(\mathbf{x}_{vBBP}) + k^2(\mathbf{x}_{vBBP}) = \mathbf{e}_{vBBP}^T \mathbf{T}(\mathbf{x}_{vBBP}, \mathbf{e}_{vBBP})\mathbf{e}_{vBBP} = g^2(\mathbf{x}_{vBBP}). \tag{A2}$$

5. *Proposed algorithm to find* $\mathbf{e}_{vBBP}$. The set of Eqs. (23), (A1), and (A2) gives the necessary and sufficient conditions to find the $\mathbf{e}_{vBBP}$ vector. A way to solve this system of equations is to find the eigenvector of the null eigenvalue of the matrix,

$$\overline{\mathbf{T}}(\mathbf{x}_{vBBP}, \mathbf{e}_{vBBP}) = \mathbf{T}(\mathbf{x}_{vBBP}, \mathbf{e}_{vBBP}) - \mathbf{z}(\mathbf{x}_{vBBP}, \mathbf{e}_{vBBP}) \times \mathbf{z}^T(\mathbf{x}_{vBBP}, \mathbf{e}_{vBBP}). \tag{A3}$$

Let $\boldsymbol{\tau}$ be the eigenvector of the null eigenvalue of the $\overline{\mathbf{T}}(\mathbf{x}_{vBBP}, \mathbf{e}_{vBBP})$ matrix; if the dot product $\boldsymbol{\tau}^T\mathbf{z}(\mathbf{x}_{vBBP}, \mathbf{e}_{vBBP}) \neq k(\mathbf{x}_{vBBP})$, then we rotate $\boldsymbol{\tau}$ such that Eq. (A1) is satisfied, being this rotated $\boldsymbol{\tau}$ vector the $\mathbf{e}_{vBBP}$ vector. Note that Eq. (23) is automatically satisfied after doing the appropriated rotation. This process is repeated until the variation on the $\mathbf{e}_{vBBP}$ vector is smaller than a given threshold.
6. *Selection of the OEEF.* This step is identical to *item* (5) of the PMED algorithm. Changing $\mathbf{x}_{oBBP}$ by $\mathbf{x}_{vBBP}$ in Eq. (23), Eqs. (A1) and (A2) give the necessary and sufficient conditions to find the $\mathbf{e}_{vBBP}$ vector; however, as in the previous algorithm, solving this problem, we get many solutions. We take the $\mathbf{e}_{vBBP}$ vector that lowers the value of the $P_{\mathbf{e}_n}(\mathbf{x}_{vBBP}, E_{vBBP})$ function. The normalization of the selected $\mathbf{e}_{vBBP}$ vector gives the $\mathbf{e}_n$ normalized direction and the norm E_{vBBP}. The integration of the corresponding FDSP curve is carried out using Eq. (8) and this normalized direction starting from the point $(\mathbf{x}_{vBBP}, E_{vBBP})$.

Finally, we consider the general case consisting in the transformation of a point $\mathbf{x}$ of the original PES $V(\mathbf{x})$ where $\mathbf{g}(\mathbf{x}) \neq \mathbf{0}$ to a BBP point of the effective or perturbed PES, $V_{\mathbf{e}_n}(\mathbf{x}_{BBP}, E_{BBP})$. It is important to recall that for this point at the effective PES, it holds that the gradient $\nabla_{\mathbf{x}} V_{\mathbf{e}_n}(\mathbf{x}_{BBP}, E_{BBP}) = \mathbf{0}$ and $\det[\mathbf{H}_{\mathbf{e}_n}(\mathbf{x}_{BBP}, E_{BBP})] = 0$. The algorithm to make this transformation is analogous to the two previous algorithms for oBBP and vBBP but with the following changes.

1. *Given a point* $\mathbf{x}$ *to be transformed to* $\mathbf{x}_{BBP}$. A point $\mathbf{x}$ should be given where $\mathbf{g}(\mathbf{x}) \neq \mathbf{0}$. We denote by $\mathbf{w}$ a vector that can be either the gradient, $\mathbf{g}(\mathbf{x})$, or an arbitrary tangent vector, $\dot{\mathbf{x}}$; in both cases, this vector $\mathbf{w}$ plays the role of tangent of the FDSP curve. Also the Hessian matrix should be computed $\mathbf{H}(\mathbf{x})$. The first and second derivatives with respect to $\mathbf{x}$ of $\{d_i(\mathbf{x})\}_{i=x,y,z}$ and $\{a_{ij}(\mathbf{x})\}_{i,j=x,y,z}$ should be computed at this selected point and be sure that simultaneously are not zero.
2. *Imposing the condition that the* $\mathbf{x}_{BBP}$ *point belongs to the FDSP.* This step is similar to *item* (2) of the first algorithm by changing $\mathbf{x}_{oBBP}$ by $\mathbf{x}_{BBP}$.
3. *The expectation value condition at* $\mathbf{x}_{BBP}$. At $\mathbf{x}_{BBP}$, Eq. (19b) should be satisfied with $k(\mathbf{x}_{BBP}) = \mathbf{w}^T\mathbf{H}(\mathbf{x}_{BBP})\mathbf{w}/(\mathbf{w}^T\mathbf{w})$. Thus, Eq. (24) now is

$$k(\mathbf{x}_{BBP}) = \mathbf{e}_{BBP}^T \mathbf{z}(\mathbf{x}_{BBP}, \mathbf{e}_{BBP}). \tag{A4}$$

Here, $k(\mathbf{x}_{BBP})$ has the value previously computed.

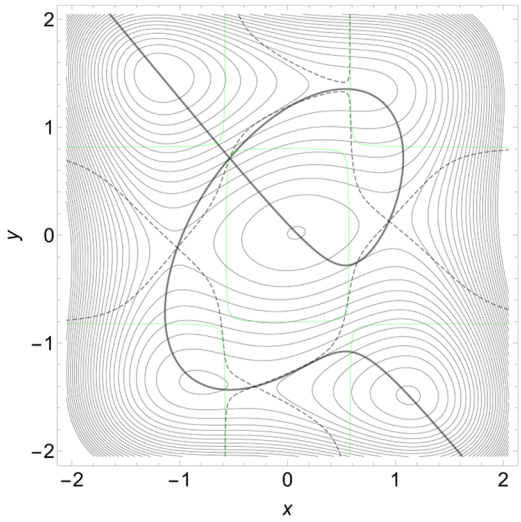

FIG. 13. Equipotential lines of the Wolfe-Quapp PES.[113,114] The bold curve is the singular NT with constant direction $(0.476, -0.879)$. This NT curve passes through the VRI point located at $(x_{VRI}, y_{VRI}) = (-0.493, 0.814)$. The green line corresponds to the manifold of points where $\det[\mathbf{H}(x,y)] = 0$; the dashed-line is the valley-ridged border line.[108]

4. *The condition* $\mathbf{k}(\mathbf{x}_{BBP}) \neq \mathbf{0}$. At the $\mathbf{x}_{BBP}$ point, Eq. (19a) is satisfied with $\mathbf{k}(\mathbf{x}_{BBP}) \neq \mathbf{0}$. In this case, Eq. (27) now is

$$\mathbf{k}^T(\mathbf{x}_{BBP})\mathbf{k}(\mathbf{x}_{BBP}) + k^2(\mathbf{x}_{BBP}) = \mathbf{e}_{BBP}^T\mathbf{T}(\mathbf{x}_{BBP}, \mathbf{e}_{BBP})\mathbf{e}_{BBP}. \tag{A5}$$

We recall that the vector $\mathbf{k}(\mathbf{x}_{BBP})$ is computed as follows:

$$\mathbf{k}(\mathbf{x}_{BBP}) = \left(\mathbf{I} - \frac{\mathbf{w}\mathbf{w}^T}{\mathbf{w}^T\mathbf{w}}\right)\mathbf{H}(\mathbf{x}_{BBP})\frac{\mathbf{w}}{\sqrt{\mathbf{w}^T\mathbf{w}}}. \tag{A6}$$

5. *Proposed algorithm to find* $\mathbf{e}_{BBP}$. The set of Eqs. (23), (A4), and (A5) gives necessary and sufficient conditions to find the $\mathbf{e}_{BBP}$ vector. A way to solve this system of equation is to find the $\mathbf{e}_{vBBP}$ vector.
6. *Selection of the OEEF.* This step is identical to *item* (5) of the first algorithm. Changing $\mathbf{x}_{oBBP}$ by $\mathbf{x}_{BBP}$ in Eq. (23), Eqs. (A4) and (A5) give the necessary and sufficient conditions to find the $\mathbf{e}_{BBP}$ vector; however, as in the previous algorithm, solving this problem, we get many solutions. We take the $\mathbf{e}_{BBP}$ vector that lowers the value of $P_{\mathbf{e}_n}(\mathbf{x}_{BBP}, E_{BBP})$ function. The normalization of the selected $\mathbf{e}_{BBP}$ vector gives the $\mathbf{e}_n$ normalized direction and the norm E_{BBP}. The integration of the corresponding FDSP curve is carried out using Eq. (8) and this normalized direction starting from the point $(\mathbf{x}_{BBP}, E_{BBP})$.

APPENDIX B: A TWO-DIMENSIONAL EXAMPLE WHERE A VRI POINT IS TRANSFORMED INTO A BBP BY MEANS OF AN APPLIED OEEF

As noted in Appendix A, in a general manner, we can say that a BBP defines the force in magnitude and direction that should be applied to a molecular system to promote a given chemical transformation by means of an electric field. In this section, we show using a two-dimensional toy model the case where the BBP corresponds to a VRI point of the original PES. The general algorithm that transforms a VRI point to a BBP is already explained in Appendix A. For this purpose, we use the Wolfe-Quapp toy PES,[113,114] see Fig. 13, for the constant dipolar field in the direction of the left upper VRI point located at $(x_{VRI}, y_{VRI}) = (-0.493, 0.814)$. We select the NT curve with constant direction $(0.476, -0.879)$, which is a singular NT and meets the former VRI point. Note that this VRI point is located in the left upper corner of the PES. If one choses a fixed, but strong enough, OEEF in this direction, one can overcome the VRI point and the stationary point of index 2 behind the VRI and open a single channel for the reaction from the upper left to the lower down minimum. We use now the dipole $\mathbf{d}^T(x,y) = (d_x(x,y), d_y(x,y)) = (0.476x, -0.879y)$ and add the new part, the perturbation poten-

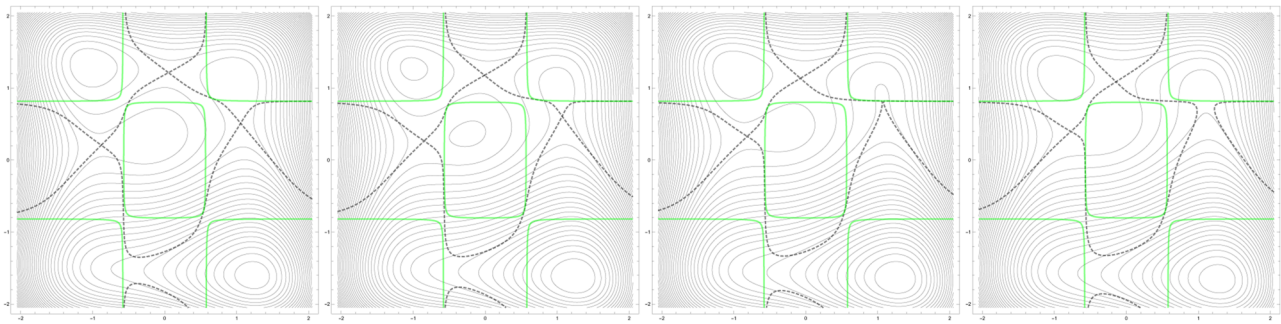

FIG. 14. Different effective PESs, $V_{\mathbf{e}_n}(x,y,E)$, from the perturbation of the Wolfe-Quapp PES, with different field strengths: from left to right, $E = 5.13$, $E = 5.98$, $E = 6.84$, and $E_{vBBP} = 7.69$. The strength of the field is given in arbitrary units. Comparing $V(x,y)$ of Fig. 13 with $V_{\mathbf{e}_n}(x,y,E)$ for $E = E_{vBBP}$, we see that the two original valleys joining the upper and left minima disappear, and a single channel opening a new direct reaction emerges. The green line corresponds to the manifold of points where $\det[\mathbf{H}_{\mathbf{e}_n}(x,y,E)] = \det[\mathbf{H}(x,y)] = 0$; the dashed-line is the valley-ridged border line.[108]

tial, $P_{\mathbf{e}_n}(x,y,E) = -E(e_x,e_y)^T\mathbf{d}(x,y)$, to form the effective new PES, $V_{\mathbf{e}_n}(x,y,E)$. Thus, each point of a FDSP path satisfies the equation

$$\begin{aligned}\mathbf{g}(x,y) &= \begin{pmatrix} g_x(x,y) \\ g_y(x,y)\end{pmatrix} = -\mathbf{m}_{\mathbf{e}_n}(x,y,E)\\ &= [\nabla_{(x,y)}(d_x(x),d_y(y))]\begin{pmatrix} e_x \\ e_y\end{pmatrix}E\\ &= \begin{pmatrix} 0.476 & 0.0 \\ 0.0 & -0.879\end{pmatrix}\begin{pmatrix} e_x \\ e_y\end{pmatrix}E = \begin{pmatrix} 0.476e_x \\ -0.879e_y\end{pmatrix}E, \qquad \text{(B1)}\end{aligned}$$

where $g_x(x,y)$ and $g_y(x,y)$ are the components of the Wolfe-Quapp PES gradient vector. In this case, the Hessian matrix of the Wolfe-Quapp PES $\mathbf{H}(x,y) \neq \mathbf{O}$, whereas the Hessian matrix of the perturbation $\mathbf{F}_{\mathbf{e}_n}(x,y,E) = \mathbf{O}$, where $\mathbf{O}$ is the zero matrix of dimension 2×2; thus, $\mathbf{H}_{\mathbf{e}_n}(x,y,E) = \mathbf{H}(x,y)$. This implies that through a FDSP path, the Wolfe-Quapp PES, $V(x,y)$, and the perturbation potential $P_{\mathbf{e}_n}(x,y,E)$ have contact of order one. For this reason, to compute the electric field, only the first item of the algorithm should be satisfied. Taking into account this fact, the (non-normalized) OEEF is trivially computed from Eq. (B1) at the VRI point, now taken as BBP, given rise the expressions $\varepsilon_x^v = g_x(x_{vBBP}, y_{vBBP})/0.476 = 5.476$ and $\varepsilon_y^v = -g_y(x_{vBBP}, y_{vBBP})/0.879 = 5.401$ in arbitrary units. The normalization of this OEEF vector gives the constant direction of the field $\mathbf{e}_n^T = (e_x, e_y) = (0.712, 0.702)$. The normalization factor is the intensity of the OEEF at the VRI point, $E_{vBBP} = 7.69$, in arbitrary units. Taking the normalized OEEF and different intensities, $E = 5.13, 5.98, 6.84, 7.69$, we obtain different contour plots of the effective PES exposed in Fig. 14. As we can see in $V_{\mathbf{e}_n}(x,y,E)$ for $E = E_{vBBP}$, the two valleys from the upper left minimum disappear, and a single channel opens for a direct reaction.

REFERENCES

[1] J. Andrés, A. Lledós, M. Duran, and J. Bertrán, "Electric fields acting as catalysts in chemical reactions. An *ab initio* study of the Walden inversion reaction," Chem. Phys. Lett. **153**, 82–86 (1988).

[2] E. Carbonell, M. Duran, A. Lledos, and J. Bertran, "Catalysis of Friedel-Crafts reactions by electric fields," J. Phys. Chem. **95**, 179–183 (1991).

[3] R. Meir, H. Chen, W. Lai, and S. Shaik, "Oriented electric fields accelerate Diels-Alder reactions and control the *endo*/*exo* selectivity," ChemPhysChem **11**, 301–310 (2010).

[4] S. Shaik, S. P. de Visser, and D. Kumar, "External electric field will control the selectivity of enzymatic-like bond activations," J. Am. Chem. Soc. **126**, 11746–11749 (2004).

[5] H. Hirao, H. Chen, M. A. Carvajal, Y. Wang, and S. Shaik, "Effect of external electric fields on the C–H bond activation reactivity of nonheme iron-oxo reagents," J. Am. Chem. Soc. **130**, 3319–3327 (2008).

[6] A. C. Aragonès, N. L. Haworth, N. Darwish, S. Ciampi, N. J. Bloomfield, G. G. Wallace, I. Diez-Pérez, and M. L. Coote, "Electrostatic catalysis of a Diels-Alder reaction," Nature **531**, 88–91 (2016).

[7] S. Shaik, D. Mandal, and R. Ramanan, "Oriented electric fields as future smart reagents in chemistry," Nat. Chem. **8**, 1091–1098 (2016).

[8] S. Shaik, R. Ramanan, D. Danovich, and D. Mandal, "Structure and reactivity/selectivity control by oriented-external electric fields," Chem. Soc. Rev. **47**, 5125–5145 (2018).

[9] S. Shaik, D. Danovich, J. Joy, Z. Wang, and T. Stuyver, "Electric-field mediated chemistry: Uncovering and exploiting the potential of (oriented) electric fields to exert chemical catalysis and reaction control," J. Am. Chem. Soc. **142**, 12551–12562 (2020).

[10] F. Che, J. T. Gray, S. Ha, N. Kruse, S. L. Scott, and J.-S. McEwen, "Elucidating the roles of electric fields in catalysis: A perspective," ACS Catal. **8**, 5153–5174 (2018).

[11] L. Zhang, E. Laborda, N. Darwish, B. B. Noble, J. H. Tyrell, S. Pluczyk, A. P. Le Brun, G. G. Wallace, J. Gonzalez, M. L. Coote, and S. Ciampi, "Electrochemical and electrostatic cleavage of alkoxyamines," J. Am. Chem. Soc. **140**, 766–774 (2018).

[12] X. Huang, C. Tang, J. Li, L.-C. Chen, J. Zheng, P. Zhang, J. Le, R. Li, X. Li, J. Liu, Y. Yang, J. Shi, Z. Chen, M. Bai, H.-L. Zhang, H. Xia, J. Cheng, Z. Tian, and W. Hong, "Electric field-induced selective catalysis of single-molecule reaction," Sci. Adv. **5**, eaaw3072 (2019).

[13] Y. Zang, Q. Zou, T. Fu, F. Ng, B. Fowler, J. Yang, H. Li, M. L. Steigerwald, C. Nuckolls, and L. Venkataraman, "Directing isomerization reactions of cumulenes with electric fields," Nat. Commun. **10**, 4482 (2019).

[14] J. Lin, Y. Lv, K. Song, X. Song, H. Zang, P. Du, Y. Zang, and D. Zhu, "Cleavage of non-polar C(sp^2)-C(sp^2) bonds in cycloparaphenylenes via electric field-catalyzed electrophilic aromatic substitution," Nat. Commun. **14**, 293–299 (2023).

[15] B. Zhang, C. Schaack, C. R. Prindle, E. A. Vo, M. Aziz, M. L. Steigerwald, T. C. Berkelbach, C. Nuckolls, and L. Venkataraman, "Electric fields drive bond homolysis," Chem. Sci. **14**, 1769–1774 (2023).

[16] X. Wang, B. Zhang, B. Fowler, L. Venkataraman, and T. Rovis, "Alkane solvent-derived acylation reaction driven by electric fields," J. Am. Chem. Soc. **145**, 11903–11906 (2023).

[17] C. Yang, Z. Liu, Y. Li, S. Zhou, C. Lu, Y. Guo, M. Ramirez, Q. Zhang, Y. Li, Z. Liu, K. N. Houk, D. Zhang, and X. Guo, "Electric field-catalyzed single-molecule Diels-Alder reaction dynamics," Sci. Adv. **7**, eabf0689 (2021).

[18] S. Ciampi, N. Darwish, H. M. Aitken, I. Díez-Pérez, and M. L. Coote, "Harnessing electrostatic catalysis in single molecule, electrochemical and chemical systems: A rapidly growing experimental tool box," Chem. Soc. Rev. **47**, 5146–5164 (2018).

[19] M. Akamatsu, N. Sakai, and S. Matile, "Electric-field-assisted anion-π catalysis," J. Am. Chem. Soc. **139**, 6558–6561 (2017).

[20] Y. B. Vogel, L. Zhang, N. Darwish, V. R. Gonçales, A. Le Brun, J. J. Gooding, A. Molina, G. G. Wallace, M. L. Coote, J. Gonzalez, and S. Ciampi, "Reproducible flaws unveil electrostatic aspects of semiconductor electrochemistry," Nat. Commun. **8**, 2066 (2017).

[21] C. F. Gorin, E. S. Beh, Q. M. Bui, G. R. Dick, and M. W. Kanan, "Interfacial electric field effects on a carbene reaction catalyzed by Rh porphyrins," J. Am. Chem. Soc. **135**, 11257–11265 (2013).

[22] M. Klinska, L. M. Smith, G. Gryn'ova, M. G. Banwell, and M. L. Coote, "Experimental demonstration of pH-dependent electrostatic catalysis of radical reactions," Chem. Sci. **6**, 5623–5627 (2015).

[23] M. T. Blyth and M. L. Coote, "A pH-switchable electrostatic catalyst for the Diels-Alder reaction: Progress toward synthetically viable electrostatic catalysis," J. Org. Chem. **84**, 1517–1522 (2019).

[24] N. G. Léonard, R. Dhaoui, T. Chantarojsiri, and J. Y. Yang, "Electric fields in catalysis: From enzymes to molecular catalysts," ACS Catal. **11**, 10923–10932 (2021).

[25] *Effects of Electric Fields on Structure and Reactivity, New Horizons in Chemistry*, Theoretical and Computational Chemistry Series, edited by S. Shaik and T. Stuyver (The Royal Society of Chemistry, 2021), pp. 001–428.

[26] T. Stuyver, D. Danovich, J. Joy, and S. Shaik, "External electric field effects on chemical structure and reactivity," Wiley Interdiscip. Rev.: Comput. Mol. Sci. **10**, e1438 (2020).

[27] Z. Wang, D. Danovich, R. Ramanan, and S. Shaik, "Oriented-external electric fields create absolute enantioselectivity in Diels-Alder reactions: Importance of the molecular dipole moment," J. Am. Chem. Soc. **140**, 13350–13359 (2018).

[28] H. M. Aitken and M. L. Coote, "Can electrostatic catalysis of Diels-Alder reactions be harnessed with pH-switchable charged functional groups?," Phys. Chem. Chem. Phys. **20**, 10671–10676 (2018).

[29] K. Bhattacharyya, S. Karmakar, and A. Datta, "External electric field control: Driving the reactivity of metal-free azide-alkyne click reactions," Phys. Chem. Chem. Phys. **19**, 22482–22486 (2017).

[30]S. Yu, P. Vermeeren, T. A. Hamlin, and F. M. Bickelhaupt, "How oriented external electric fields modulate reactivity," Chem. - Eur. J. **27**, 5683–5693 (2021).
[31]P. Besalú-Sala, M. Solà, J. M. Luis, and M. Torrent-Sucarrat, "Fast and simple evaluation of the catalysis and selectivity induced by external electric fields," ACS Catal. **11**, 14467–14479 (2021).
[32]R. Ramanan, D. Danovich, D. Mandal, and S. Shaik, "Catalysis of methyl transfer reactions by oriented external electric fields: Are gold-thiolate linkers innocent?," J. Am. Chem. Soc. **140**, 4354–4362 (2018).
[33]E. J. Mattioli, A. Bottoni, F. Zerbetto, and M. Calvaresi, "Oriented external electric fields affect rate and stereoselectivity of electrocyclic reactions," J. Phys. Chem. C **123**, 26370–26378 (2019).
[34]T. Stuyver, D. Danovich, F. De Proft, and S. Shaik, "Electrophilic aromatic substitution reactions: Mechanistic landscape, electrostatic and electric-field control of reaction rates, and mechanistic crossovers," J. Am. Chem. Soc. **141**, 9719–9730 (2019).
[35]J. Joy, T. Stuyver, and S. Shaik, "Oriented external electric fields and ionic additives elicit catalysis and mechanistic crossover in oxidative addition reactions," J. Am. Chem. Soc. **142**, 3836–3850 (2020).
[36]C. Acosta-Silva, J. Bertran, V. Branchadell, and A. Oliva, "Kemp elimination reaction catalyzed by electric fields," ChemPhysChem **21**, 295–306 (2020).
[37]Y. Chen, Y. Liu, Q. Zhang, Y. Yan, and W. Yin, "Degradation of bromobenzene via external electric field," J. Theor. Comput. Chem. **19**, 2050004 (2020).
[38]J. Wu, T. Long, H. Wang, J.-X. Liang, and C. Zhu, "Oriented external electric fields regurating the reaction mechanism of CH_4 oxidation catalyzed by Fe(IV)-Oxo-Corrolazine: Insight from density functional calculations," Front. Chem. **10**, 896944 (2022).
[39]F. Che, J. T. Gray, S. Ha, and J.-S. McEwen, "Improving Ni catalysts using electric fields: A DFT and experimental study of the methane steam reforming reaction," ACS Catal. **7**, 551–562 (2017).
[40]E. M. Kempfer-Robertson and L. M. Thompson, "Effect of oriented external electric fields on the photo and thermal isomerization of azobenzene," J. Phys. Chem. A **124**, 3520–3529 (2020).
[41]K. Jutglar Lozano, R. Santiago, J. Ribas-Arino, and S. T. Bromley, "Twistable dipolar aryl rings as electric field actuated conformational molecular switches," Phys. Chem. Chem. Phys. **23**, 3844–3855 (2021).
[42]T. Stuyver and S. Shaik, "Resolving entangled reactivity modes through external electric fields and substitution: Application to E_2/S_N2 reactions," J. Org. Chem. **86**, 9030–9039 (2021).
[43]M. Zhang, W. Li, Z. Zhou, S. Zhuo, and Z. Su, "Green catalytic method for hydrothiolation of allylamines: An external electric field," ACS Omega **7**, 5782–5790 (2022).
[44]H. R. Kelly, P. E. Videla, C. P. Kubiak, T. Lian, and V. S. Batista, "Controlling hydricity of adsorbed catalysts with applied electric fields," J. Phys. Chem. C **127**, 6733–6743 (2023).
[45]D. J. Hanaway and C. R. Kennedy, "Automated variable electric-field DFT application for evaluation of optimally oriented electric fields on chemical reactivity," J. Org. Chem. **88**, 106–115 (2023).
[46]P. Besalú-Sala, A. A. Voityuk, J. M. Luis, and M. Solà, "Effect of external electric fields in the charge transfer rates of donor–acceptor dyads: A straightforward computational evaluation," J. Chem. Phys. **158**, 244111 (2023).
[47]A. Warshel, P. K. Sharma, M. Kato, Y. Xiang, H. Liu, and M. H. M. Olsson, "Electrostatic basis for enzyme catalysis," Chem. Rev. **106**, 3210–3235 (2006).
[48]S. D. Fried, S. Bagchi, and S. G. Boxer, "Extreme electric fields power catalysis in the active site of ketosteroid isomerase," Science **346**, 1510–1514 (2014).
[49]S. D. Fried and S. G. Boxer, "Electric fields and enzyme catalysis," Annu. Rev. Biochem. **86**, 387–415 (2017).
[50]A. Bhowmick, S. C. Sharma, and T. Head-Gordon, "The importance of the scaffold for *de novo* enzymes: A case study with Kemp eliminase," J. Am. Chem. Soc. **139**, 5793–5800 (2017).
[51]M. Dittner and B. Hartke, "Globally optimal catalytic fields-inverse design of abstract embeddings for maximum reaction rate acceleration," J. Chem. Theory Comput. **14**, 3547–3564 (2018).
[52]V. V. Welborn and T. Head-Gordon, "Fluctuations of electric fields in the active site of the enzyme ketosteroid isomerase," J. Am. Chem. Soc. **141**, 12487–12492 (2019).
[53]V. V. Welborn, L. Ruiz Pestana, and T. Head-Gordon, "Computational optimization of electric fields for better catalysis design," Nat. Catal. **1**, 649–655 (2018).
[54]M. Dittner and B. Hartke, "Globally optimal catalytic fields for a Diels-Alder reaction," J. Chem. Phys. **152**, 114106 (2020).
[55]T. Stuyver, R. Ramanan, D. Mallick, and S. Shaik, "Oriented (local) electric fields drive the millionfold enhancement of the H-abstraction catalysis observed for synthetic metalloenzyme analogues," Angew. Chem., Int. Ed. **59**, 7915–7920 (2020).
[56]C. Zheng, Y. Mao, J. Kozuch, A. O. Atsango, Z. Ji, T. E. Markland, and S. G. Boxer, "A two-directional vibrational probe reveals different electric field orientations in solution and an enzyme active site," Nat. Chem. **14**, 891–897 (2022).
[57]W. Peng, S. Yan, X. Zhang, L. Liao, J. Zhang, S. Shaik, and B. Wang, "How do preorganized electric fields function in catalytic cycles? The case of the enzyme tyrosine hydroxylase," J. Am. Chem. Soc. **144**, 20484–20494 (2022).
[58]Here, it is worth to recall that the IUPAC defines *catalysis* as the action of a *catalyst*, a substance that increases the rate of a chemical reaction without modifying the overall $\Delta_r G^0$ of the process. The catalyst is both a reactant and a product of the reaction. In this sense, the use of the term *electrostatic catalysis* to describe the effect of an OEEF to promote a given chemical reaction is somewhat misleading since there is no such substance. For this reason, the expression *electrostatic catalytic effects* is used in this work to describe the process of reduction of reaction barriers (or its annihilation in the optimal case) using OEEFs.
[59]J. M. Bofill, W. Quapp, G. Albareda, I. de P. R. Moreira, and J. Ribas-Ariño, "A model for an optimally oriented external electric field to control the chemical reaction path: A generalisation of the Newton trajectory," J. Chem. Theory Comput. **18**, 935–952 (2022).
[60]J. M. Bofill, W. Quapp, G. Albareda, I. de P. R. Moreira, J. Ribas-Ariño, and M. Severi, "A catastrophe theory-based model for optimal control of chemical reactions by means of oriented electric fields," Theor. Chem. Acc. **142**, 22–35 (2023).
[61]W. Quapp, J. M. Bofill, and J. Ribas-Ariño, "Towards a theory of mechanochemistry-simple models from the early beginnings," Int. J. Quantum Chem. **118**, e25775 (2018).
[62]J. Stroscio and D. Eigler, "Atomic and molecular manipulation with the scanning tunneling microscope," Science **254**, 1319–1326 (1991).
[63]S. Yan, X. Ji, W. Peng, and B. Wang, "Evaluating the transition state stabilization/destabilization effects of the electric fields from scaffold residues by a QM/MM approach," J. Phys. Chem. B **127**, 4245–4253 (2023).
[64]C. Carathéodory, *Calculus of Variations and Partial Differential Equations of the First Order* (Chelsea Publishing Company, New York, 1982).
[65]J. Pancíř, "Calculation of the least energy path on the energy hypersurface," Collect. Czech. Chem. Commun. **40**, 1112–1118 (1975).
[66]M. Basilevsky and A. Shamov, "The local definition of the optimum ascent path on a multi-dimensional potential energy surface and its practical application for the location of saddle points," Chem. Phys. **60**, 347–358 (1981).
[67]D. J. Rowe and A. Ryman, "Valleys and fall lines on a Riemannian manifold," Math. Phys. **23**, 732–735 (1982).
[68]M. Basilevsky, "The topography of potential energy surfaces," Chem. Phys. **67**, 337–346 (1982).
[69]D. K. Hoffman, R. S. Nord, and K. Ruedenberg, "Gradient extremals," Theor. Chim. Acta **69**, 265–279 (1986).
[70]W. Quapp, "Gradient extremals and valley floor bifurcation on potential energy surfaces," Theor. Chim. Acta **75**, 447–460 (1989).
[71]D. Heidrich, W. Kliesch, and W. Quapp, *Properties of Chemically Interesting Potential Energy Surfaces* (Springer, Berlin, Heidelberg, 1991).
[72]H. B. Schlegel, "Following gradient extremal paths," Theor. Chim. Acta **83**, 15–20 (1992).
[73]J.-Q. Sun and K. Ruedenberg, "Gradient extremals and steepest descent lines on potential energy surfaces," J. Chem. Phys. **98**, 9707–9714 (1993).
[74]K. Bondensgård and F. Jensen, "Gradient extremal bifurcation and turning points: An application to the H_2CO potential energy surface," J. Chem. Phys. **104**, 8025–8031 (1996).
[75]J. M. Bofill, W. Quapp, and M. Caballero, "The variational structure of gradient extremals," J. Chem. Theory Comput. **8**, 927–935 (2012).

[76]J. M. Bofill, J. Ribas-Ariño, S. P. García, and W. Quapp, "An algorithm to locate optimal bond breaking points on a potential energy surface for applications in mechanochemistry and catalysis," J. Chem. Phys. **147**, 152710 (2017).
[77]J. M. Bofill, R. Valero, J. Ribas-Ariño, and W. Quapp, "Barnes update applied in the Gauss-Newton method: An improved algorithm to locate bond breaking points," J. Chem. Theory Comput. **17**, 996–1007 (2021).
[78]W. Quapp and J. M. Bofill, "A contribution to a theory of mechanochemical pathways by means of Newton trajectories," Theor. Chem. Acc. **135**, 113–129 (2016).
[79]K. Fukui, "A formulation of the reaction coordinate," J. Phys. Chem. **74**, 4161–4163 (1970).
[80]W. Quapp and D. Heidrich, "Analysis of the concept of minimum energy path on the potential energy surface of chemically reacting systems," Theor. Chim. Acta **66**, 245–260 (1984).
[81]P. Valtazanos and K. Ruedenberg, "Bifurcations and transition states," Theor. Chim. Acta **69**, 281–307 (1986).
[82]W. Quapp, "How does a reaction path branching take place? A classification of bifurcation events," J. Mol. Struct. **695-696**, 95–101 (2004).
[83]W. Quapp and B. Schmidt, "An empirical, variational method of approach to unsymmetric valley-ridge inflection points," Theor. Chem. Acc. **128**, 47–61 (2011).
[84]J. Bofill and W. Quapp, "Analysis of the valley-ridge inflection points through the partitioning technique of the Hessian eigenvalue equation," J. Math. Chem. **51**, 1099–1115 (2013).
[85]F. Neese, "The ORCA program system," Wiley Interdiscip. Rev.: Comput. Mol. Sci. **2**, 73–78 (2012).
[86]F. Neese, "Software update: The ORCA program system, version 4.0," Wiley Interdiscip. Rev.: Comput. Mol. Sci. **8**, e1327 (2018).
[87]F. Neese, F. Wennmohs, U. Becker, and C. Riplinger, "The ORCA quantum chemistry program package," J. Chem. Phys. **152**, 224108 (2020).
[88]F. Neese, "Software update: The ORCA program system–Version 5.0," Wiley Interdiscip. Rev.: Comput. Mol. Sci. **12**, e1606 (2022).
[89]F. Neese, "The SHARK integral generation and digestion system," J. Comput. Chem. **44**, 381–396 (2023).
[90]J. M. Bofill, W. Quapp, J. Ribas-Ariño, M. Severi, G. Albareda, and I. de P. R. Moreira, MANULS (Make chemicAl reactioNs spontaneoUs via optimaL fieldS).
[91]M. Severi, MANULS, 2023.
[92]G. Berthier, "Configurations électroniques incomplètes," J. Chim. Phys. **51**, 363–371 (1954).
[93]J. A. Pople and R. K. Nesbet, "Self-consistent orbitals for radicals," J. Chem. Phys. **22**, 571–572 (1954).
[94]W. J. Hehre, R. Ditchfield, and J. A. Pople, "Self–consistent molecular orbital methods. XII. Further extensions of Gaussian–type basis sets for use in molecular orbital studies of organic molecules," J. Chem. Phys. **56**, 2257–2261 (1972).
[95]Here, we opted for using UHF in the broken symmetry approach as a cost-effective multireferential model to describe the isomerization curve because the TS associated with the isomerization process of cumulene has a multireference character (as opposed to the TS of the Huisgen reaction). However, we acknowledge that B3LYP-D3 has been demonstrated to perform well when modeling the activation energy for the *cis-trans* isomerization of closely related cumulene derivatives.[96] Note that the results reported in this subsection are not meant to provide the most accurate possible results for the E-field-induced annihilation of the isomerization barrier of cumulene, but to show an application of the PMED model coupled with the wavefunction methodology.
[96]M. U. Bühringer, K. Padberg, M. D. Phleps, H. Maid, C. Placht, C. Neiss, M. J. Ferguson, A. Görling, and R. R. Tykwinski, "Double bonds? Studies on the barrier to rotation about the cumulenic C=C bonds of tetraaryl[*n*]cumulenes (n = 3, 5, 7, 9)," Angew. Chem., Int. Ed. **57**, 8321–8325 (2018).
[97]F. Neese, F. Wennmohs, A. Hansen, and U. Becker, "Efficient, approximate and parallel Hartree–Fock and hybrid DFT calculations. A 'chain-of-spheres' algorithm for the Hartree–Fock exchange," Chem. Phys. **356**, 98–109 (2009).
[98]A. D. Becke, "Density-functional thermochemistry. III. The role of exact exchange," J. Chem. Phys. **98**, 5648–5652 (1993).
[99]C. Lee, W. Yang, and R. G. Parr, "Development of the Colle-Salvetti correlation-energy formula into a functional of the electron density," Phys. Rev. B **37**, 785–789 (1988).
[100]S. H. Vosko, L. Wilk, and M. Nusair, "Accurate spin-dependent electron liquid correlation energies for local spin density calculations: A critical analysis," Can. J. Phys. **58**, 1200–1211 (1980).
[101]P. J. Stephens, F. J. Devlin, C. F. Chabalowski, and M. J. Frisch, "*Ab initio* calculation of vibrational absorption and circular dichroism spectra using density functional force fields," J. Phys. Chem. **98**, 11623–11627 (1994).
[102]F. Weigend and R. Ahlrichs, "Balanced basis sets of split valence, triple zeta valence and quadruple zeta valence quality for H to Rn: Design and assessment of accuracy," Phys. Chem. Chem. Phys. **7**, 3297–3305 (2005).
[103]S. Grimme, J. Antony, S. Ehrlich, and H. Krieg, "A consistent and accurate *ab initio* parametrization of density functional dispersion correction (DFT-D) for the 94 elements H–Pu," J. Chem. Phys. **132**, 154104 (2010).
[104]S. Grimme, S. Ehrlich, and L. Goerigk, "Effect of the damping function in dispersion corrected density functional theory," J. Comput. Chem. **32**, 1456–1465 (2011).
[105]W. Quapp, M. Hirsch, and D. Heidrich, "Bifurcation of reaction pathways: The set of valley ridge inflection points of a simple three-dimensional potential energy surface," Theor. Chem. Acc. **100**, 285–299 (1998).
[106]M. Hirsch, W. Quapp, and D. Heidrich, "The set of valley-ridge inflection points on the potential energy surface of water," Phys. Chem. Chem. Phys. **1**, 5291–5299 (1999).
[107]W. Quapp and V. Melnikov, "The set of valley ridge inflection points on the potential energy surfaces of H_2S, H_2Se and H_2CO," Phys. Chem. Chem. Phys. **3**, 2735–2741 (2001).
[108]W. Quapp, M. Hirsch, and D. Heidrich, "An approach to reaction path branching using valley-ridge inflection points of potential energy surfaces," Theor. Chem. Acc. **112**, 40–51 (2004).
[109]B. Schmidt and W. Quapp, "Search of manifolds of nonsymmetric valley-ridge inflection points on the potential energy surface of HCN," Theor. Chem. Acc. **132**, 1305–1313 (2012).
[110]W. Quapp, J. Bofill, and A. Aguilar-Mogas, "Exploration of cyclopropyl radical ring opening to allyl radical by Newton trajectories: Importance of valley-ridge inflection points to understand the topography," Theor. Chem. Acc. **129**, 803–821 (2011).
[111]W. Quapp and J. Bofill, "Topography of cyclopropyl radical ring opening to allyl radical on the CASSCF(3,3) surface: Valley-ridge inflection points by Newton trajectories," J. Math. Chem. **50**, 2061–2085 (2012).
[112]W. Quapp, "Can we understand the branching of reaction valleys for more than two degrees of freedom?," J. Math. Chem. **54**, 137–148 (2015).
[113]S. Wolfe, H. B. Schlegel, I. G. Csizmadia, and F. Bernardi, "Chemical dynamics of symmetric and asymmetric reaction coordinates," J. Am. Chem. Soc. **97**, 2020–2024 (1975).
[114]W. Quapp, "A growing string method for the reaction pathway defined by a Newton trajectory," J. Chem. Phys. **122**, 174106 (2005).